

Article

Quench and Tempered Embrittlement of Ultra-High-Strength Steels with Transition Carbides

Roman Mishnev ^{1,2} , Yuliya Borisova ^{1,2} , Tatiana Kniaziuk ^{1,3}, Sergey Gaidar ¹ and Rustam Kaibyshev ^{1,*}

¹ Laboratory of Advanced Steels for Agricultural Machinery, Russian State Agrarian University–Moscow Timiryazev Agricultural Academy, 127550 Moscow, Russia; mishnev@bsu.edu.ru (R.M.); borisova_yu@bsu.edu.ru (Y.B.)

² Laboratory of Mechanical Properties of Nanostructured Materials and Superalloys, Belgorod State National Research University, 308015 Belgorod, Russia

³ National Research Center “Kurchatov Institute”–Central Research Institute of Structural Materials “Prometey”, 191015 St. Petersburg, Russia

* Correspondence: kajbyshev@rgau-msha.ru; Tel.: +7-4722-585455; Fax: +7-4722-585417

Abstract: The effect of tempering after water quenching on the strength and fracture toughness of two steels with chemical compositions of 0.34%C-1.77%Si-1.35Mn-0.56%Cr-0.2%Mo-0.04%Nb-0.03Ti-0.002B and 0.44%C-1.81%Si-1.33%Mn-0.82%Cr-0.28%Mo was examined. The last steel exhibits quenching embrittlement in an as-quenched condition. At a tempering temperature of 280 °C, the precipitation of transition η -Fe₂C carbides in martensitic matrix leads to increasing fracture toughness and eliminates quench embrittlement in the steel with 0.44 wt.%C. Tempered martensite embrittlement at 400 °C appears as decreased values of the Charpy V-notch impact energy, ductility and the product of strength and elongation, $\sigma_B \times \delta$ (MPa × %) and is attributed to increased effective grain size for fracture, mainly. The precipitation of boundary cementite takes place at tempering at 500 °C and provides increased ductility and fracture toughness despite a decohesion along carbide/ferrite interfaces. The low severity of TME in Si-rich low-alloy medium carbon steels is attributed to the suppression of boundary cementite precipitation at tempering temperatures ≤ 400 °C.

Keywords: tempered martensite embrittlement; quenching and tempering; low-alloy steel; mechanical properties; microstructure; phase transformation; carbides

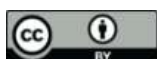


Citation: Mishnev, R.; Borisova, Y.; Kniaziuk, T.; Gaidar, S.; Kaibyshev, R.

Quench and Tempered Embrittlement of Ultra-High-Strength Steels with Transition Carbides. *Metals* **2023**, *13*, 1399. <https://doi.org/10.3390/met13081399>

Academic Editors: Atef Saad Hamada, Jesús Toribio, Beatriz González and Francisco-Javier Ayaso

Received: 29 June 2023
Revised: 29 July 2023
Accepted: 3 August 2023
Published: 5 August 2023



Copyright: © 2023 by the authors. Licensee MDPI, Basel, Switzerland. This article is an open access article distributed under the terms and conditions of the Creative Commons Attribution (CC BY) license (<https://creativecommons.org/licenses/by/4.0/>).

1. Introduction

Structural steels capable of exhibiting a yield stress (YS) of ≥ 1380 MPa/200 ksi are referred to as ultra-high-strength steels (UHSS) [1,2]. Low-alloy UHSS with transition carbides are widely used in the aerospace industry and are considered to be advanced materials for the transportation industry and agricultural machinery [1,2]. These steels are produced by quenching followed by low-temperature tempering that provides high strength, sufficient ductility, excellent fatigue resistance, and high resistance to abrasion and wear [1–4]. However, these steels exhibit relatively low fracture toughness and are susceptible to low-temperature embrittlement that may lead to sudden accidents [3–6]. The key disadvantage of UHSS with transition carbides is relatively low values of the Charpy V-notch (CVN) impact energy [1,7]. Sufficient ductility and fracture toughness is attained in these steels by vacuum arc remelting, the use of modified heat treatment routes, and/or alloying the steels with ≥ 1.5 wt.%Si [1,7–11]. Additions of Si ≥ 1.5 wt.% reduce significantly the precipitation of cementite which enhances the strength and toughness of UHSS [1,4,10,12–16]. The microstructure of Si-enriched UHSS consists of lath martensite with transition carbides located in the matrix and film-like retained austenite (RA) located at lath and block boundaries [1,14,17].

Low-alloy steels are susceptible, depending on chemical composition, to embrittlement after quenching and/or tempering [3]. Quench embrittlement associates with intergranular brittle fracture and takes place in steels with carbon content >0.5 wt.% in both the

as-quenched and low-temperature tempered conditions [3]. Tempered martensite embrittlement (TME) characterized by a trough in CVN impact energy at ambient temperature appears in low-alloy high-strength steels tempered at temperatures ranging from 250 to 400 °C [3,5,6,18]. It is known that TME is associated with a transgranular fracture but precise mechanisms of this phenomenon are still discussed. Several mechanisms may be responsible for TME in steels with different chemical composition: (i) the decomposition of RA to films of cementite located at lath/block boundaries [3,5,6,18,19] or $M_{23}C_6$ carbides located at boundaries of prior austenite grains (PAG) or packets [20–22]; (ii) precipitation of coarse cementite at lath boundaries [3,6,18]; and (iii) transformation of film-like RA to strain-induced martensite under dynamic loading that induces the formation of microcracks [3,6,7]. High P content promotes TME [6].

Two approaches are used to diminish TME. First, Si additions allow for avoiding TME due to suppression of the formation of coarse interlath cementite and decomposition of RA [10,23]. Alloying steels with ≥ 1.5 wt.%Si suppresses the precipitation of cementite during the decomposition of RA to bainite [24]. Since the boundary cementite particles with plate-like shape are considered as the most important TME agent [3,6,18] the suppression of cementite precipitation strongly decreases the severity of TME. Second, the severity of TME can be diminished by grain refinement [5]. The CVN impact energy of steels with martensite lath structure is controlled by values of stress for brittle fracture expressed by the following relationship [25–27]:

$$\sigma_F = 1.41 \sqrt{\frac{2E\gamma_s}{\pi(1-\nu^2)}} d_{eff}^{-1/2} \quad (1)$$

where $E = 212$ GPa is Young's modulus, γ_s is the surface energy of the cleavage plane for martensite structure, $\nu = 0.293$ is Poisson's ratio, d_{eff} is the effective grain size for fracture [27]. Different types of boundaries can inhibit crack propagation along {001} cleavage planes playing the role of obstacles for cleavage propagation. Blocks, packets and PAGs [22] may play a role in the effective grain size, d_{eff} , for toughness [5]. It is known [28,29] that the dimension of packets is about five times higher than the size of blocks and the size of PAG is higher than that of packets by a factor ranging from 3 to 8. Therefore, if the propagation of the micro-crack is arrested and stopped at the block boundaries instead of the boundaries of packets or PAGs, the fracture stress and fracture toughness tend to increase [5,30]. It is worth noting that the Bain unit boundaries acting as obstacles for cleavage crack propagation in lath martensite structure strongly enhance high fracture toughness [30].

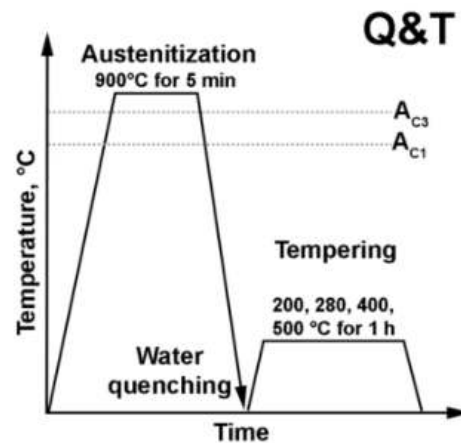
The main aim of the present study is to consider the mechanism of TME in Si-enriched UHSSs. Additions of Si ≥ 1.5 wt.% suppress the formation of cementite below ~ 450 °C [29,30]. Almost no boundary carbides precipitate in these steels up to ~ 450 °C [20,29]. No cementite appears due to the decomposition of RA occurring at $T \leq 400$ °C [20,29], that is, in contrast with steels with Si ≤ 0.5 wt.% [3,6,7,10,14,19,31]. In addition, the volume fraction of RA after water quenching in these steels is negligible ($\sim 1\%$). Therefore, we can expect that a unique mechanism of TME is operative in these steels. The second aim is to evaluate the susceptibility of the UHSS with ≥ 1.5 wt.%Si to quench embrittlement.

2. Materials and Methods

The chemical compositions of two experimental steels, denoted here as Fe-0.34C and Fe-0.44C, are listed in Table 1. These steels were produced by air induction melting followed by electro-slag remelting. Next, the steels were subjected to solution treatment at 1150 °C for 4 h, followed by forging at temperatures from 1150 to 950 °C into billets with dimensions of $60 \times 150 \times 450$ mm³ with subsequent air cooling. Samples were subjected to austenitization at 900 °C for 5 min followed by water quenching. The pre-hold time at the austenitization temperature was 1 min per 1 mm sample thickness. Isochronal tempering was carried out at 200, 280, 400 and 500 °C for 1 h with subsequent air cooling. (Figure 1).

Table 1. Chemical composition of steels in wt.%.

Steel	C	Si	Mn	Cr	Mo	Nb	Ti	P	S
Fe-0.34C	0.34	1.77	1.35	0.56	0.2	0.04	0.03	0.006	0.006
Fe-0.44C	0.44	1.81	1.33	0.82	0.28	-	-	0.007	0.001

**Figure 1.** Schematic graphs of Q&T treatments.

Hardness was measured using a Wolpert Wilson 600 MRD (Illinois ToolWorks Inc., Norwood, MA, USA) tester in accordance with ASTM E18 Standard at room temperature. At least five measurements of each specimen were conducted. The flat specimens with a gauge length of 35 mm and a cross-section of $7 \times 3 \text{ mm}^2$ were cut from the quenched and tempered steels and then tensioned using an Instron 5882 testing machine (Illinois ToolWorks Inc., Norwood, MA, USA) at room temperature and an initial loading rate of 1 mm/min in accordance with ASTM E08M-04 Standard. Standard CVN specimens were tested at room temperature using the Instron SI-1M impact machine with a maximum energy of 450 J with the Instron Dynatup Impulse data acquisition system following the ASTM E-23 Standard. At least two standard-tensile and CVN specimens of each condition were tested.

Structural characterization was carried out using a Quanta 600 FEG scanning electron microscope (SEM) (FEI Corporation, Hillsboro, OR, USA) equipped with an electron backscatter diffraction (EBSD) pattern analyzer incorporated with an orientation imaging microscopy (OIM) system and a JEOL JEM-2100 (JEOL Ltd., Tokyo, Japan) transmission electron microscope (TEM). Foils for TEM studies were prepared by double-jet electropolishing using a solution of 10% perchloric acid in glacial acetic acid under a voltage of 21.0 V at an ambient temperature. The surfaces of the specimens for SEM observation were mechanically polished and then electropolished using the same electrolyte. These specimens were examined by the EBSD technique. The OIM images were subjected to a clean-up procedure, setting the minimal confidence index to 0.1. The low- (LAB) and high-angle (HAB) boundaries were defined with misorientations of $2^\circ \leq \theta < 15^\circ$ and $\geq 15^\circ$, respectively, and depicted in the OIM images using white and black lines, respectively. Densities of lattice dislocations were calculated from misorientation maps obtained by the EBSD technique using Kernel average misorientation [32]:

$$\rho_{KAM} = \frac{2\theta_{KAM}}{b \cdot h} \quad (2)$$

where b is the Burgers vector, the distance h corresponds to the step size of the scanning. The ρ_{KAM} value characterizes the elastic bending of the crystal lattice and, therefore, internal elastic stress fields [32]. The misorientation maps obtained by the EBSD technique were processed to reconstruct PAGs using the open-source crystallographic toolbox MTEX 5.8 with the software suite ORTools [29,33,34]. The identification of packets by variant

selection was performed using the technique of parent grain reconstruction described by Niessen et al. [33]. The fractured surfaces of the tension and CVN specimens were observed using the Quanta 600 FEG SEM. Crack propagation in the CVN specimens was analyzed on the fractured specimens by EBSD on lateral surfaces [35]. Other details of structural and mechanical characterization were reported in previous works [16,17,20,29,35,36].

The volume fraction of RA was determined by magnetic saturation measurements using Fischer Feritscope FMP30 (Helmut Fischer GmbH, Sindelfingen, Germany). Differential scanning calorimetry (DSC) was performed using an SDT Q600 (TA Instruments New Castle, DE, USA) calorimeter. The mass of samples was ~142 mg, and a protective atmosphere of pure argon was used. Samples austenitized at a temperature of 900 °C and, finally, water-quenched were heated from 20 to 550 °C at a rate of 10 °C/min. The dilatometry curves were obtained during cooling from 900 °C to room temperature at a cooling rate of 100 °C/s using a DIL 805 dilatometer of the same company on cylindrical samples with a 10 mm length and a 3 mm diameter to determine the M_S and M_F temperatures. In addition, rod-shaped samples with a length of 25 mm and a diameter of 6 mm were cooled from 905 °C to ambient temperature at a rate of 5 °C/min using a DIL 402C dilatometer of the same company to determine A_{C1} and A_{C3} temperatures.

3. Results

3.1. Dilatometry, DSC Analysis, Magnetic Saturation Measurements and Critical Temperatures

The A_{C1} , A_{C3} , martensite-start (M_S) and martensite-finish (M_F) critical temperatures of two steels determined by dilatometry are listed in Table 2. It is seen that if the A_{C1} temperatures are nearly the same for two steels the A_{C3} , M_S and M_F temperatures for the Fe-0.34C steel are higher than those for the Fe-0.44C steel. Since A_{C3} temperatures < 900 °C for two steels (Table 2), the full austenitization took place under heat treatment.

Table 2. Critical temperatures.

Steel	A_{C1} , °C	A_{C3} , °C	M_S , °C	M_F , °C
Fe-0.34C	761	886	316	140
Fe-0.44C	766	857	270	51

The high M_F temperature of the Fe-0.34C steel corresponds with a negligible volume fraction of RA after quenching and the increased volume fraction of RA in the Fe-0.44C steels correlates with M_F temperature close to the ambient one (Tables 3 and 4).

Table 3. Microstructural parameters of the Fe-0.34C steel after quenching and tempering.

Tempering Temperature, °C	PAG Size, μm	Packet Size, μm	Block Thickness, μm	Distance between HABs, μm	Lath Thickness, nm	$\rho_{KAM} \times 10^{14}, \text{m}^{-2}$	Volume Fraction of RA, %
20	23 ± 5	6.2 ± 1.5	0.53 ± 0.08	0.91 ± 0.13	209 ± 33	9.4	0.8
200	26 ± 4	8.5 ± 1.9	0.49 ± 0.08	0.98 ± 0.14	216 ± 34	9.1	0.6
280	27 ± 6	9.3 ± 2.1	0.65 ± 0.09	0.98 ± 0.14	234 ± 29	9.3	0.5
400	26 ± 6	8.6 ± 1.7	0.63 ± 0.07	1 ± 0.14	231 ± 35	8.4	0.4
500	23 ± 3	6.5 ± 1.2	0.52 ± 0.08	1 ± 0.14	235 ± 33	8.6	0.2

Table 4. Microstructural parameters of the Fe-0.44C steel after quenching and tempering.

Tempering Temperature, °C	PAG Size, μm	Packet Size, μm	Block Thickness, μm	Distance between HABs, μm	Lath Thickness, nm	$\rho_{KAM} \times 10^{14}, \text{m}^{-2}$	Volume Fraction of RA, %
20	30 ± 5	11.5 ± 1.5	0.59 ± 0.15	0.86 ± 0.11	179 ± 29	9.5	3.9 ± 0.2
200	34 ± 3	10 ± 1.5	0.64 ± 0.12	0.9 ± 0.13	194 ± 30	7.8	2.8 ± 0.3
280	31 ± 5	8 ± 2	0.58 ± 0.12	0.7 ± 0.12	216 ± 32	8.5	1.1 ± 0.5
400	31 ± 4	7 ± 2	0.52 ± 0.19	0.72 ± 0.1	223 ± 29	8.7	0
500	35 ± 3	9.5 ± 1.5	0.65 ± 0.15	0.65 ± 0.15	243 ± 34	8.3	0

The DSC analysis (not shown here) supports previous data [29]. The precipitation of transition carbides and cementite takes place at ~200 and ~475 °C, respectively, in two steels.

Si additions strongly increase the precipitation temperature of cementite as compared to low-Si steels with similar carbon content [3,7,10]. The volume fraction of RA in the Fe-0.34 steel is negligible (Table 3) and the effect of RA decomposition on a dispersion of carbide is insignificant. In the Fe-0.44 steel, an almost four times decrease in volume fraction of RA takes place after tempering at 280 °C, and full decomposition of RA was detected at 400 °C (Table 4).

3.2. Microstructure

Typical microstructures of the Fe-0.34C steel after water quenching and tempering at 500 °C are presented in Figure 2a,b and structural parameters are summarized in Table 3. Microstructures after isochronal tempering at the other temperatures are not shown here since the effect of tempering temperatures ranging from 200 to 400 °C on the microstructure is insignificant. Martensite lath structure exhibiting typical three-level hierarchy in its morphology, i.e., PAGs, packets and blocks [22,28] evolved after quenching. Nb additions provided relatively small dimensions of PAGs exhibiting round shapes (Table 3, Figure 2(a,a1)). The ratio between the average dimensions of PAG and packets is $D_{packet} = 0.27 \times D_{PAG}$, the ratio between dimensions of the packet and block thickness is $d_{block} \sim 0.085 \times D_{packet}$, and the ratio between dimensions of PAGs and block thickness is $d_{block} \sim 0.023 \times D_{PAG}$ (Table 3). These ratios are inconsistent with ones of $D_{packet} = 0.4 \times D_{PAG}$ and $d_{block} \sim 0.067 \times D_{PAG}$ ensuring that the net strain in the PAG is pure dilatation in order to accommodate the lattice distortions associated with $\gamma \rightarrow \alpha'$ transformation [28,37,38]. It was assumed [28,37] that the following relationships between PAGs, packets and blocks have to be fulfilled:

$$D_{Packet} = \sqrt{\frac{3\sqrt{3}}{8N_p}} D_{PAG} \quad (3)$$

$$d_{block} = \frac{1}{N_b} D_{Packet} \quad (4)$$

where N_p is the number of packets in a PAG, N_b is the number of blocks in a packet. These relationships predict unrealistically high N_p and N_b values in the Fe-0.34C steel. Therefore, the crystallography-based relationships interlinking the PAG, packet and block do not obey Equations (3) and (4) suggested in [28]. The high elastic stress associated with ρ_{KAM} value (Table 3) is present in quenched structure since elastic strain energy attributed to shape changes during martensitic transformation is dictated by the number of variants in the Kurdjumov–Sachs (K–S) $\{111\}_\gamma \parallel \{011\}_{\alpha'} \langle 110 \rangle_\gamma \parallel \langle 111 \rangle_{\alpha'}$ orientation relationship (OR) [28,37,38]. The lowest strain fields in martensite lath structure are achieved if packets with four different $\{111\}_\gamma$ planes are formed in a PAG and six variants of the K–S OR appear in a packet [28,37,38].

An inspection of misorientation maps (Figure 2(a,a2)) shows that the number of packets with lattice belonging to different $\{111\}_\gamma$ planes is three or even less in the majority of PAGs with dimensions $\leq 20 \mu\text{m}$. These PAGs contain one coarse packet with a round shape (Table 3) and fine rectangular packets consisting of two or even one block. Therefore, refinement of PAGs induces long-range elastic stress fields in martensitic structure due to the lack of four possible habit $\{111\}_\gamma$ planes in fine PAGs. Three types of packets are distinctly distinguished in the martensite lath structure. First, the PAGs with dimensions $> 20 \mu\text{m}$ contain six or more packets belonging to four different habit $\{111\}_\gamma$ planes, and these packets contain typically more than three blocks (Figure 2(a1,a2)). It is worth noting that these coarse packets exhibiting rectangular shapes comprise six or more blocks with six K–S variants. This is typical for high-carbon steel with $\geq 0.61 \text{ wt.\%C}$ [22,39]. The second type is fine packets with irregular shapes comprising ~ 3 blocks with different K–S OR, and each block consists of two sub-blocks with specific K–S variants [22,34]. In summary, the fine packets contain six K–S OR. These packets are typical for low-to-medium carbon steels with $\leq 0.38 \text{ wt.\%C}$ [39]. The invalidity of relationships (3) and (4) is attributed to the third type of packets containing two blocks or even one block. Therefore, these packets

contain four or less K-S OR. In the small PAGs, a coarse packet with one $\{111\}_\gamma$ habit plane is subdivided to separate packets by the inclination of packets belonging to the third type and characterized by the other $\{111\}_\gamma$ habit plane (Figure 2(a1,a2)).

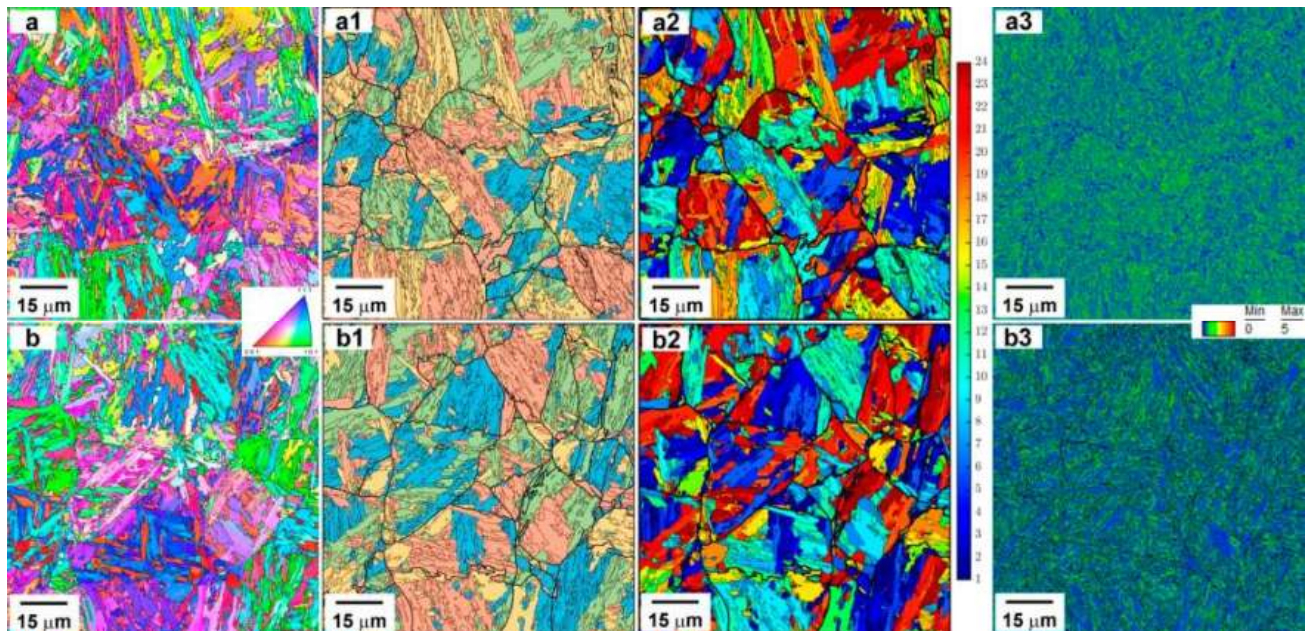


Figure 2. EBSD analysis of the Fe-0.34C steel after quenching (a–a3) and tempering at 500 °C (b–b3): (a,b) misorientation maps; (a1,b1) misorientation map showing HABs of the reconstructed PAGs and packets; (a2,b2) the K–S variant maps (in the K–S variant maps, black lines denote the reconstructed PAG boundaries); (a3,b3) KAM maps.

The first and second types of packets are characterized by lower elastic strain energy since these packets may be composed of six K-S OR. The KAM patterns (Figure 2(a3)) support this conclusion. Lattice distortions in these packets are relatively low (Figure 2(a3)). Strong internal distortions are observed in packets containing less than four specific K–S variant groups (Figure 2(a3)). Film-like RA is located along the lath boundaries, but its volume fraction is negligible (Table 3).

Tempering affects martensite lath structure insignificantly. Changes in the dimensions of PAGs, packets, blocks and the ρ_{KAM} values lie in accuracy limits (Table 3). In contrast, the lath thickness tends to increase with increasing temperature of tempering up to 500 °C (Table 3). However, the increment in lath thickness lies also within measurement accuracy (Table 3). Tempering at 280 °C decreases lattice distortions in the coarse packets containing six blocks. After tempering at 400 °C the lattice distortions decrease in almost all packets with six specific K–S variant groups. After tempering at 500 °C the lattice distortions become small in block pairs adjacent to boundaries of PAGs and packets (Figure 2(b1,b2)).

The size of PAGs in the Fe-0.44C steel is higher than that in the Fe-0.34C steel (Tables 3 and 4, Figure 3). Packets exhibit rectangular shapes and the number of packets with different habit $\{111\}_\gamma$ planes is three in a major portion of PAGs (Figure 3(a,a2)). In addition, a block with the other habit $\{111\}_\gamma$ plane could be distinguished within these PAGs, and, therefore, four possible variants of the $\{111\}_\gamma$ planes are present in the majority of PAGs. Three aforementioned types of packets are also observed. The feature of this steel is a high number (>6) of blocks per coarse packet (Figure 3). Packets consisting of one block are rarely observed (Figure 3(b2)). Therefore, the effect of Si additions and carbon content on the morphology of packets is nearly the same [39]. It is obvious that packet morphology in the Fe-0.44C steel is typical for high-carbon steel with ≥ 0.61 wt.%C [39].

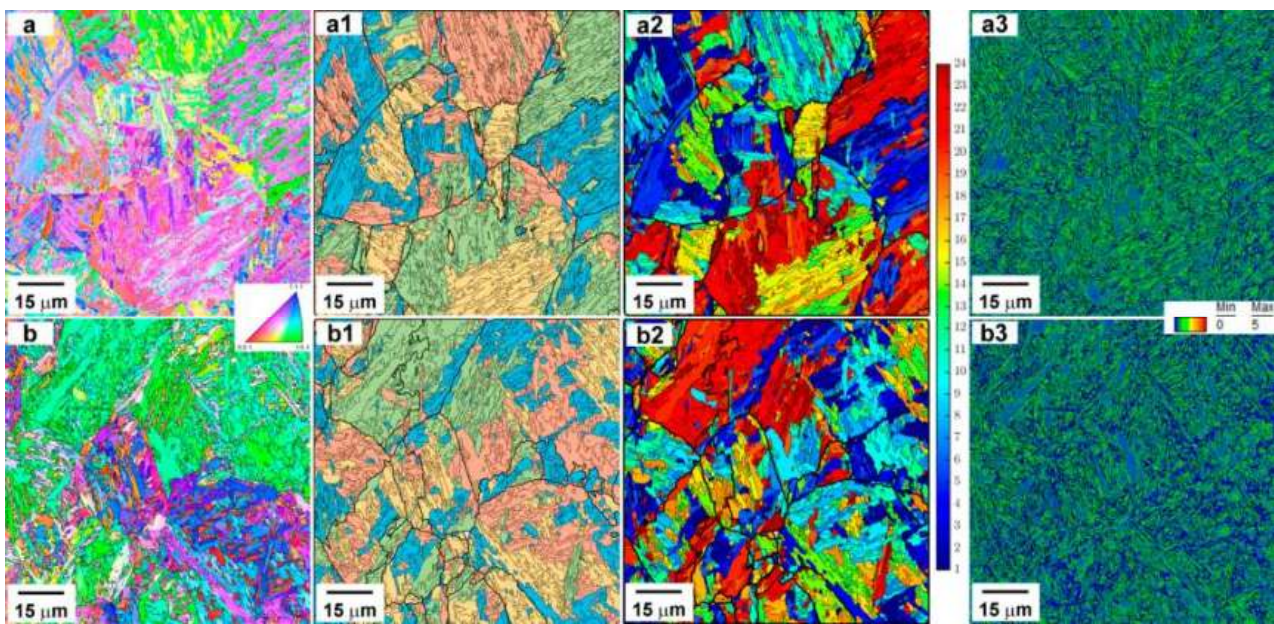


Figure 3. EBSD analysis of the Fe-0.44C steel after quenching (a–a3) and tempering at 500 °C (b–b3): (a,b) misorientation maps; (a1,b1) misorientation map showing HAGBs of the reconstructed PAGs and packets; (a2,b2) the K–S variant maps (In the K–S variant maps, black lines denote the reconstructed PAG boundaries); (a3,b3) KAM maps.

The distance between HAGBs is ~40% larger than the block thickness and, therefore, a major portion of block boundaries exhibits high-angle misorientation [22]. Following ratios between dimensions of structural elements of martensite lath structure were obtained: $D_{packet} = 0.38 \times D_{PAG}$, $d_{block} \sim 0.086 \times D_{packet}$, $d_{block} \sim 0.02 \times D_{PAG}$ (Table 4). Relationships (3) and (4) are fulfilled for $N_p = 4$ and $N_b = 11$. In contrast with the Fe-0.34C steel, these N_p and N_b values are consistent with misorientation data (Figure 2). The Fe-0.44C steel is characterized by large lattice distortions (Figure 3(a3)) that confirm the necessity of six K-S variants for the lowest elastic stress fields [22,34]. Small lattice distortions are observed in some coarse packets containing more than 5 blocks (Figure 3(a1–a3)). The volume fraction of RA in the Fe-0.44C steel is higher by a factor of ~5 than that in the Fe-0.34C steel (Tables 2 and 3). Film-like RA is dominant while the blocky-type RA with a volume fraction of ~0.7% could be also found.

Tempering leads to the decomposition of RA, lath coarsening and decreasing packet size and distance between HAGBs in the Fe-0.44C steel (Table 4). An increase in the number of HAGBs within coarse packets (Figure 3(b1,b2)) correlates with the decomposition of RA. Transformation of film-like RA to bainitic ferrite with transition carbides [16,24] produces additional HAGBs that decrease the average distance between HAGBs. A decrease in packet size is attributed to the appearance of packets containing one block within coarse packets (Figure 3(b1,b2)). The origin of this process is not clear. After tempering at 400 and 500 °C, the lattice distortions become smaller in block pairs adjacent to boundaries of PAGs and packets (Figure 3(b3)). In addition, areas exhibiting an almost round shape and very small lattice distortion appear in small packets containing no more than two blocks and located at the boundaries of PAGs (Figure 3(b3)).

3.3. Distribution of Secondary Phase Particles

Two types of secondary phase particles are observed after quenching in the Fe-0.34C steel: Nb(C,N) carbonitrides exhibiting round shape and transition η -carbide (Fe_2C) with plate-like shape with an aspect ratio (AR) of ~8 (Appendix A). Nb(C,N) carbonitrides usually precipitate on dislocations in austenite during hot working [40] and the η -carbide precipitate under autotempering [29,41]. Tempering leads to coarsening of Nb(C,N) car-

bonitrides due to the depletion of carbon and Nb from martensite and lengthening of η -carbides due to diffusion-controlled migration of incoherent edges [42] that leads to an increase in AR of plates up to ~ 19 after at 400 °C (Appendix A). No precipitation of cementite was detected at temperatures ≤ 400 °C and no overlap between precipitation of transition carbide and cementite occurs at the temperature interval 200–400 °C as in steel with low Si [41,42]. After tempering at 500 °C, the cementite particles with round shape precipitate on boundaries (Appendix A). The formation of dense chains of boundary cementite particles is accompanied by the full dissolution of transition carbides (Appendix A). In the Fe-0.34C steel, the precipitation of transition carbides and cementite takes place in two distinct temperature intervals: 200–400 °C and ≥ 474 °C, respectively. No overlap between these processes takes place in the steel with ≥ 1.5 wt.%Si at a tempering temperatures of ≤ 400 °C. The precipitation of transition carbide occurs in the martensitic matrix and nucleation of cementite on boundaries takes place independently and eventually leads to the full replacement of η -carbide by cementite in accordance with the Gibbs–Thomson effect [42].

In the Fe-0.44C steel, no carbides were found after quenching. The precipitation of transition η -carbide was rarely observed at a tempering temperature of 200 °C (Figure 4a). However, their density is small and dimensions are about twice lower than those in the Fe-0.34C steel (Figure 4a, Table 5). High-density transition carbides are observed after tempering at 280 °C in the matrix (Figure 4b). After tempering at 400 °C the formation of long plates of η -carbide is detected (Figure 4c, Table 5). No precipitation of cementite was found. Chains of cementite particles with nearly round shapes located on lath and block boundaries appear after tempering at 500 °C. Therefore, the precipitation sequence in the Fe-0.34 and Fe-0.44C steels is the same and could be presented in the form [29]:

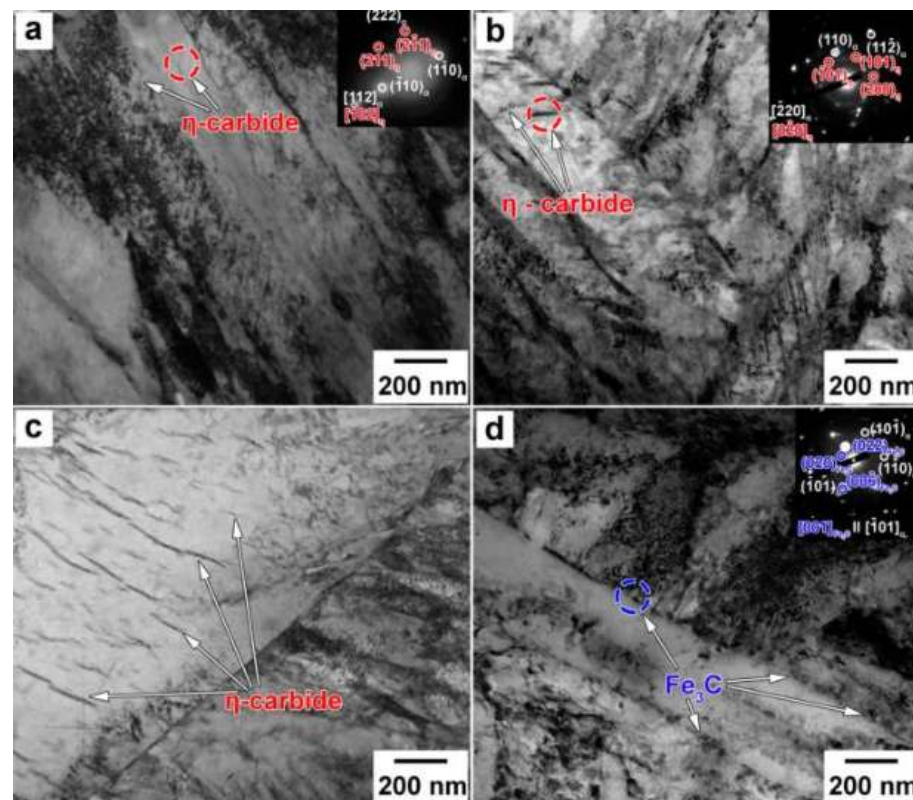
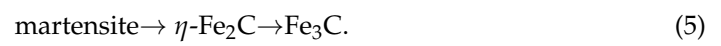


Figure 4. Typical TEM micrograph of the Fe-0.44C steel after tempering at 200 °C (a), 280 °C (b), 400 °C (c) and 500 °C (d).

Table 5. Effect of tempering on dimensions of secondary phase particles in the Fe-0.44C steel.

Tempering Temperature, °C	Dimensions of η -Fe ₂ C, nm	Size of Fe ₃ C, nm
20	-	-
200	41/3 *	-
280	98/5	-
400	108/6	-
500	-	25 ± 3

* Numerator and denominator are the particle length and thickness, respectively.

The effect of carbon on the precipitation sequence consists of the formation of additional RA. However, the decomposition of RA leads to the precipitation of transition carbides, and, therefore, this process has no effect on the origin and distribution of carbides [3,41].

3.4. Mechanical Properties

The engineering stress–strain curves of the Fe-0.34C and Fe-0.44C steels after quenching and tempering are shown in Figure 5a,b, respectively. Hardness, YS, ultimate tensile strength (UTS), uniform elongation, ductility and the product of strength and elongation (PSE) are summarized in Table 6 for the Fe-0.34C steel and Table 7 for the Fe-0.44C steel. Two steels exhibit continuous yielding [3] in all conditions. After quenching the fracture occurs immediately after yielding in the Fe-0.44C steel, while the intense strain hardening provides sufficient ductility in the Fe-0.34C steel. Therefore, the Fe-0.44C steel exhibits quench embrittlement in tension [3,43]. Increasing the temperature of tempering decreases values of strain hardening (Figure 5c,d). Tempering strongly increases the ductility of the Fe-0.44C steel and has little effect on the elongation to failure of the Fe-0.34C steel. Thus, the low-temperature tempering eliminates quench embrittlement in the Fe-0.44C steel. It is worth noting that steels with >0.5 wt.%C are brittle after low-temperature tempering [3,43] and quench embrittlement is observed after quenching, only, in the Si-enriched Fe-0.44C steel.

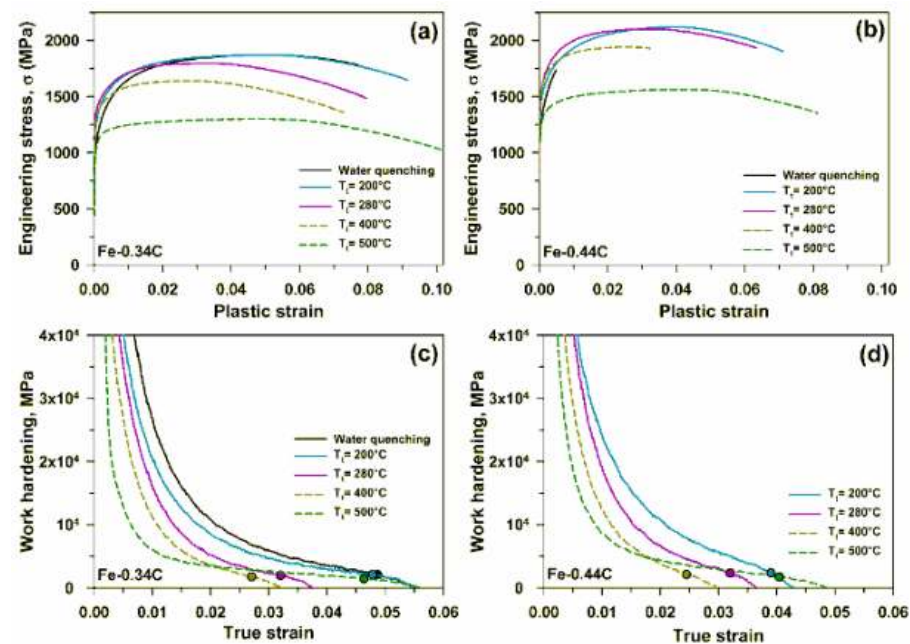


Figure 5. Typical engineering stress–strain curves (a,b) and strain hardening vs strain curves (c,d) of the Fe-0.34C steel (a,c); the Fe-0.44C steel (b,d).

Table 6. Mechanical properties of the Fe-0.34%C steel after quenching and tempering.

Tempering Temperature, °C	YS, MPa	UTS, MPa	El _u , %	El _t , %	PSE, GPa×%	HRC	CVN, J/cm ²
20	1280	1870	4.3	7.5	14	54	17
200	1430	1870	4.4	9	17	54	31
280	1490	1870	2.9	8	14.4	53	35
400	1420	1640	2.3	7.5	12.3	50	23
500	1160	1300	4.6	10.5	14	43	38

Table 7. Mechanical properties of the Fe-0.44%C steel after quenching and tempering.

Tempering Temperature, °C	YS, MPa	UTS, MPa	El _u , %	El _t , %	PSE, GPa×%	HRC	CVN, J/cm ²
20	1500	1730	0.5	0.5	-	60	6
200	1640	2120	3.9	7.5	15.5	58	12
280	1730	2100	3.1	6.5	13.6	57	14
400	1700	1940	2.5	3	6	55	9
500	1370	1560	3.7	8.5	13	47	20

Tempering at $T \leq 280$ °C increases the YS of two steels and UTS of the Fe-0.44C steel. In the Fe-0.34C steel, the UTS value remains unchanged up to a tempering temperature of 280 °C and tends to decrease at higher temperatures of tempering. As a result, increasing the temperature of tempering from 200 to 400 °C shifts the onset of the Considère condition [3]:

$$\frac{d\sigma}{d\varepsilon} = \sigma. \quad (6)$$

to low strain and decreases ductility in two steels (Figure 5c,d). The onset of the Considère criterion almost matches with UTS at these tempering temperatures and precedes necking. Uniform elongation decreases with increasing tempering temperature at $T \leq 400$ °C. At a tempering temperature of 400 °C the ductility and PSE decrease due to the lowest strain of the onset of the Considère criterion. In the Fe-0.44C steel, the necking results in immediate premature fracture, while in the Fe-0.34C steel, significant plastic deformation occurs behind the Considère strain. As a result, in the Fe-0.34C steel, the ductility and PSE are nearly independent of the tempering temperature. Tempering at 500 °C increases uniform elongation, ductility and the PSE in two steels. The Considère strains after tempering at temperatures of 200 and 500 °C are nearly the same in the two steels. The main feature of the tension behavior of the Fe-0.44C steel tempered at 500 °C is an extension of the necking stage. As a result, the PSE values of the two steels after tempering at temperatures of 280 and 500 °C are essentially the same. An increase in ductility is compensated by a decrease in UTS.

CVN impact energies of the Fe-0.34C and Fe-0.44C steels are presented in Tables 6 and 8, respectively. It is seen that the fracture toughness of the Fe-0.34C steel is higher than that of the Fe-0.44C steels by factors ranging from 2 to 4 for different conditions. The low fracture toughness of the Fe-0.44C steel in the as-quenched condition supports the occurrence of quench embrittlement [3,43]. This phenomenon manifests itself with practically zero ductility and a small CVN impact energy. In two steels, the low temperature tempering at $T \leq 280$ °C provides a two-time increase in CVN impact energy. At a tempering temperature of 400 °C the well-defined TME associated with decreased CVN impact energies is observed. Therefore, TME manifests itself in decreased values of ductility, the PSE and fracture toughness. Tempering at 500 °C increases the fracture toughness of two steels, significantly. The Fe-0.34C steel after this tempering is tough, while the Fe-0.44C steel remains relatively brittle since the CVN impact energy is smaller than 28 J [44].

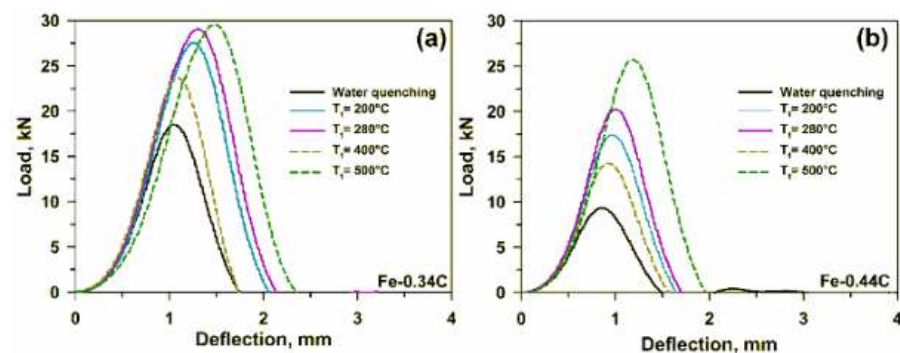
Table 8. The P_M and DUTS calculated from Charpy load–deflection curves.

Tempering Temperature, °C	P_M , kN		DUTS, MPa	
	Fe-0.34C	Fe-0.44C	Fe-0.34C	Fe-0.44C
20	18	9	711	356
200	28	17	1107	672
280	29	20	1147	790
400	23	14	909	553
500	29	25	1147	988

Load-deflection curves are shown in Figure 6. It is seen that all curves exhibit only the maximum load, P_M , point [20,29,44,45]. The P_M values of the Fe-0.34C steel are higher than those of the Fe-0.44C steel (Table 8). The increase in CVN impact energy is attributed to increased P_M value. The dynamic ultimate tensile strength (DUTS), σ_{UTSd} , can be obtained using the following relationship [20,29,45]:

$$\sigma_{UTSd} = \frac{\eta_{Pm} P_M W}{(W - a)^2 B} \quad (7)$$

where W is the specimen width (=10 mm); B is the specimen thickness (=10 mm); a is the notch depth (=2 mm); the constraint factor at maximum force $\eta_{Pm} = 2.531$ was taken for low-alloy steels [29].

**Figure 6.** Typical load–deflection curves of the Fe-0.34C steel (a) and Fe-0.44C steel (b).

The DUTS values (Table 8) are lower than even static YS (Tables 6 and 7) for all material conditions and, therefore, the onset of crack propagation takes place before dynamic yielding through brittle mechanisms. In quenched conditions, the DUTS are smaller than YS by factors of ~2 and ~4 for the Fe-0.34C and Fe-0.44C steels, respectively. Low-temperature tempering increases DUTS and the ratio of YS/DUTS decreases. Tempering at 400 °C leads to an insignificant decrease in DUTS in the Fe-0.34C steel. DUTS is 62% of YS. In the Fe-0.44C, steel tempering at 400 °C provides a 30% decrease in DUTS and DUTS/YS=0.32. It is apparent that embrittlement takes place in the Si-enriched UHSSs if DUST is smaller than 33%YS. After tempering at 500 °C the values of DUTS and YS are nearly the same in the Fe-0.34C steel and DUTS is 72% from YS in the Fe-0.44C steel. Therefore, the Si-enriched low-alloy steel becomes tough if DUTS is equal to YS.

3.5. Fractography

Figures 7 and 8 represent the overall views of the fracture surfaces of the Fe-0.34C and Fe-0.44C steels, respectively, after tensioning. After quenching, the fracture occurs almost without necking in the two steels, which is evidence of brittle behavior [46,47]. Only two well-known fracture signatures, i.e., a fibrous zone associated with crack nucleation in the center of the specimens and a shear-lip zone associated with the arrest of crack propagation at specimen edges, are observed [46–48]. The fibrous zone occupies almost 90% of the fracture surface and is characterized by quasi-cleavage fracture [3,46–48] in the

Fe-0.34C steel (Figure 7a). In coarse packets, the blocks play a role of effective grain size for fracture. Cleavage planes come across blocks, but at block boundaries, the transmission of cleavage occurs through its initiation along parallel $\{100\}_\alpha$ planes in an adjacent block. Cleavage propagates through block boundaries in fine packets playing the role of effective grain size for fracture. Thus, the propagation of microcracks is arrested by boundaries of two structural elements of martensite structure, i.e., block boundaries in coarse packets and boundaries of fine packets.

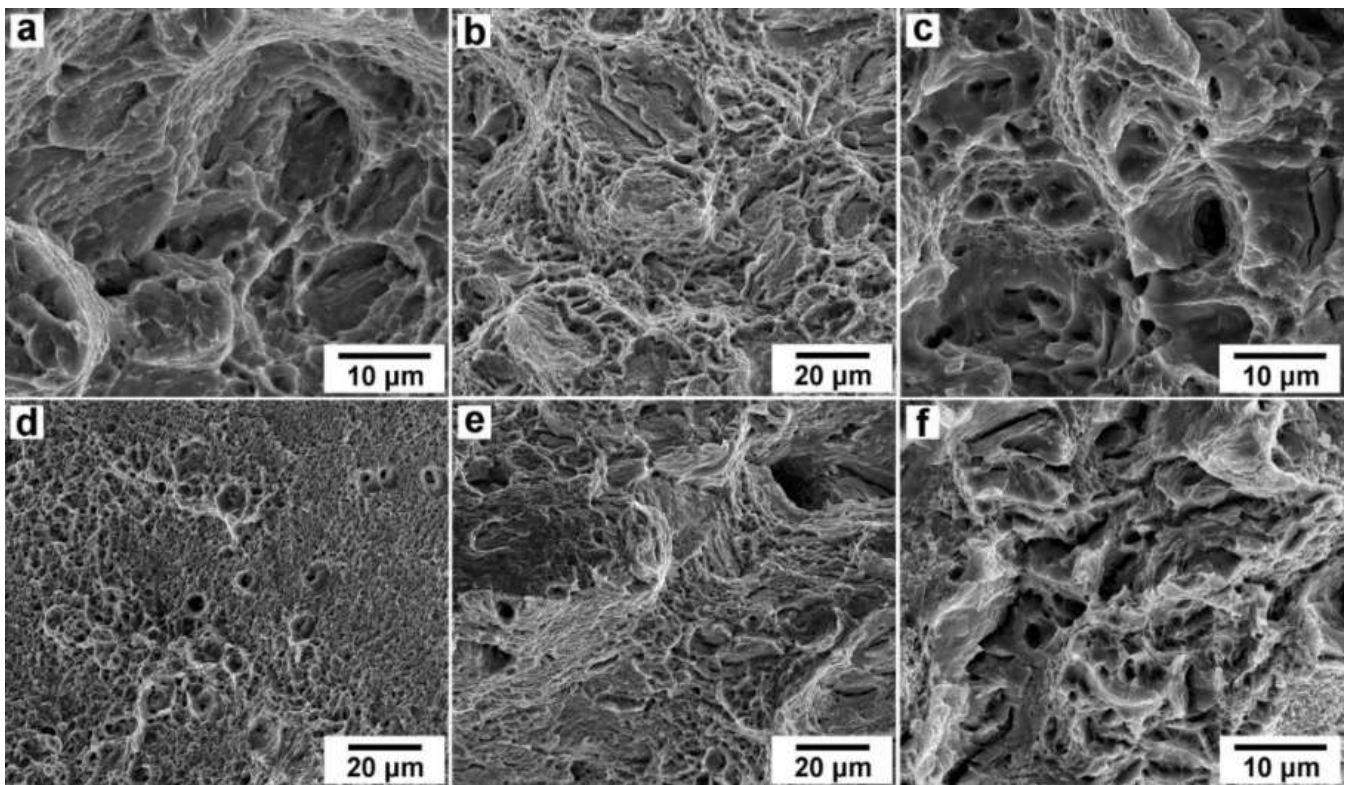


Figure 7. The fracture surfaces of the specimens machined from the Fe-0.34C steel and tensioned after quenching—fibrous zone (a); tempering at 200 °C—fibrous zone (b), tempering at 280 °C—fibrous zone (c) and shear-lip zone (d); tempering at 400 °C—fibrous zone (e); tempering at 500 °C—fibrous zone (f).

In the Fe-0.44C steel, the intergranular fracture is dominant in the center of the fracture surface (Figure 7a) and crack propagation in the fibrous zone occurs through a quasi-cleavage mechanism in transgranular fracture mode (Figure 7b) [3,46–48]. It is worth noting that intergranular fracture is a specific feature of quench embrittlement [3,43] and, therefore, this phenomenon is responsible for lacking ductility of the Fe-0.44C steel in the as-quenched condition. It is worth noting that high stress (Table 7) is necessary to initiate intergranular fracture mode. Premature crack nucleation at boundaries restricts the ductility of the Fe-0.44C steel in the quenched condition. This steel exhibits no necking.

A dimple fracture is observed in the shear-lip zone (not shown here). Tempering at 200 °C leads to necking and expanding the shear-lip zone of ductile fracture up to ~50% of the fracture surface in two steels. Mixture quasi-cleavage–dimple fracture mode is observed; block boundaries play the role of effective obstacles for stopping cleavage in the fibrous zone (Figure 7b). In the fibrous zone, the portion of ductile fracture in the Fe-0.44C steel is lower than in the Fe-0.34C steel (Figure 8b). A radial fracture zone [46–48] appears and dimple fracture becomes the main fracture mechanism in the fibrous zone in the Fe-0.34C steel. The ductile fracture mechanism plays an important role in the Fe-0.44C steel after tempering at 280 °C (Figures 7c and 8c). Shallow dimples are observed in the radial fracture zone (Figure 8d).

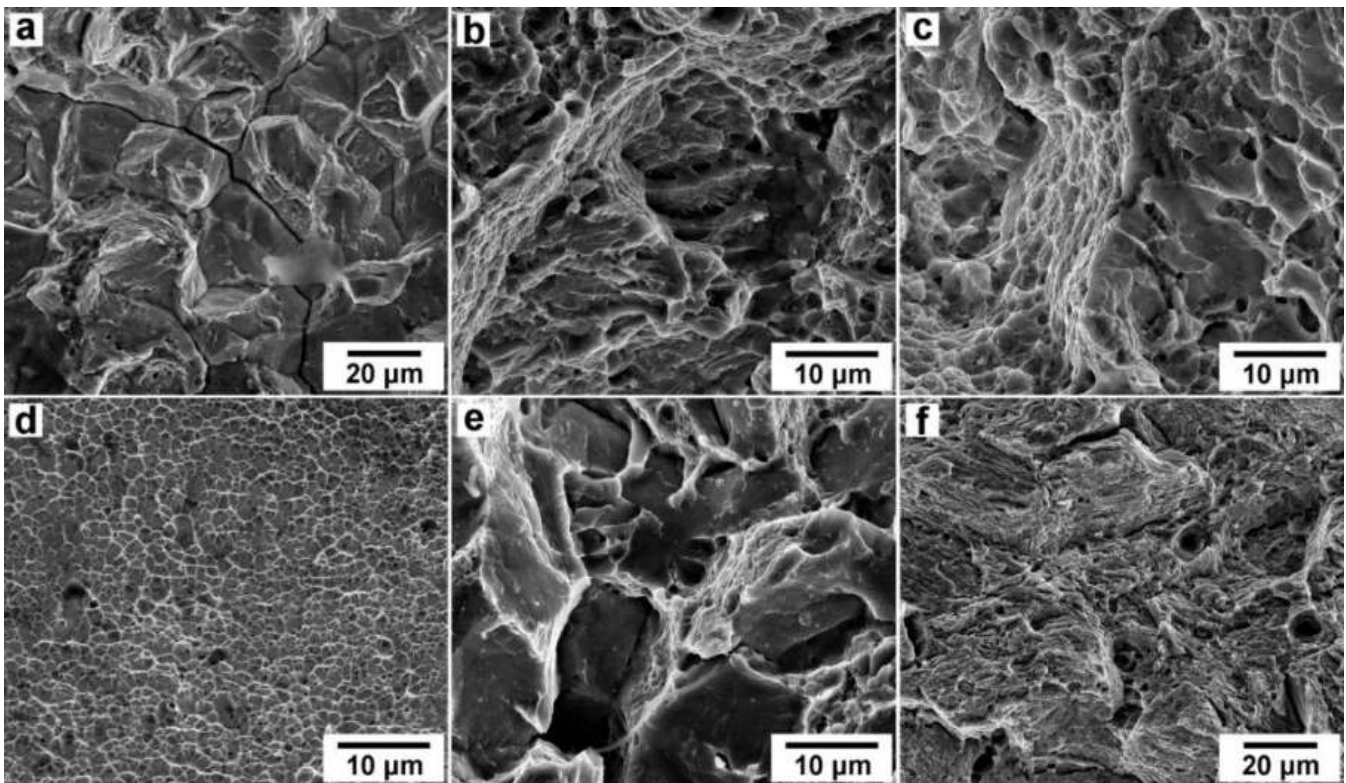


Figure 8. The fracture surfaces of the specimens machined from the Fe-0.44C steel and tensioned after quenching—fibrous zone (a); tempering at 200 °C—fibrous zone (b); tempering at 280 °C—fibrous zone (c); tempering at 280 °C—radial fracture zone (d); tempering at 400 °C—fibrous zone (e); tempering at 500 °C—fibrous zone (f).

Tempering at 400 °C decreases the contribution of dimple fracture in the fibrous zone; PAGs and coarse packets play a role of effective grain size for cleavage fracture (Figure 7e). Therefore, tempering at this temperature diminishes the role of block boundaries as stoppers for cleavage propagation. The intergranular fracture appears in the fibrous zone of the Fe-0.44C steel. In the Fe-0.34C steel, the role of this fracture mechanism is minor (Figure 7e). This steel exhibits necking, while almost no localization of plastic deformation was found in the Fe-0.44C steel. Crack nucleation and propagation take place without any necking in the Fe-0.44C steel. Therefore, the low ductility of the Fe-0.44C steel is attributed to the fact that PAGs and coarse packets play a role of effective grain size for fracture in the fibrous zone occupying ~60% of fracture surface and this induces crack nucleation under stable plastic flow. In contrast, the Fe-0.34C steel is susceptible to necking, and elongation to failure of this material is 150% higher than that of the Fe-0.44C steel despite the fact that uniform elongations of two steels are essentially the same (Tables 6 and 7). After tempering at 500 °C the transgranular dimple fracture is dominant in the Fe-0.34C steel (Figure 7f), while intergranular fracture and quasi-cleavage transgranular fracture with blocks as an effective grain size are observed in the Fe-0.44C steel in the fibrous zone (Figure 8f).

The fracture surface of CVN specimens consists of initiation zone (IZ), fast crack propagation/fibrous zone (FCPZ) and shear-lip zone (SLZ) (Figure 9) [6,44,47,49]. The effect of tempering temperature on area fractions of these zones is summarized in Table 9 and the fractographs of the V-notch Charpy specimens after impact tests are presented in Figures 10 and 11. The dimple fracture is observed in the IZ (not shown here) and ductile crack growth under plain strain conditions takes place in SLZ. Quasi-cleavage fracture takes place in the FCPZ in the Fe-0.34C in the as-quenched condition (Figure 10(a1,a2)). Packets and blocks play a role of effective grain size in the FCPZ. In the Fe-0.44C steel the propagation of microcracks stops at block boundaries in the IZ (Figure 11(a1–a3)).

Packets play a role of an effective grain size for fracture in the FCPZ and shallow dimples are observed in the SLZ. Intergranular fracture along the boundaries of some PAGs is rarely observed. In areas of FCPZ adjacent to the SLZ the cleavage occurs within blocks in addition to whole packets. Therefore, increasing stress promotes the propagation of cleavage through block boundaries and quench embrittlement manifests itself through transgranular fracture with low fracture stress in the Fe-0.44C steel.

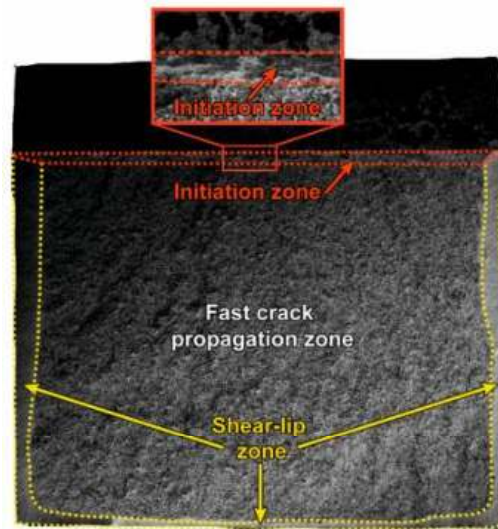


Figure 9. Schematic of fracture surfaces of the specimens machined from the Fe-0.44C steel.

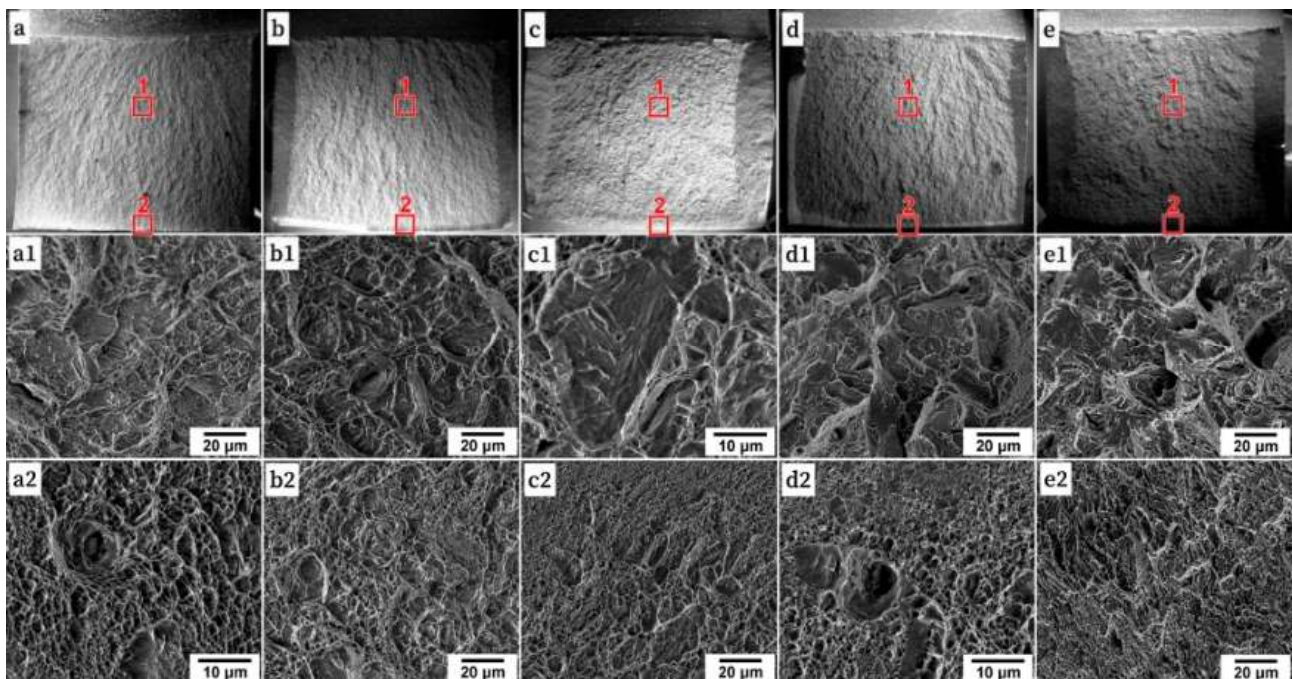
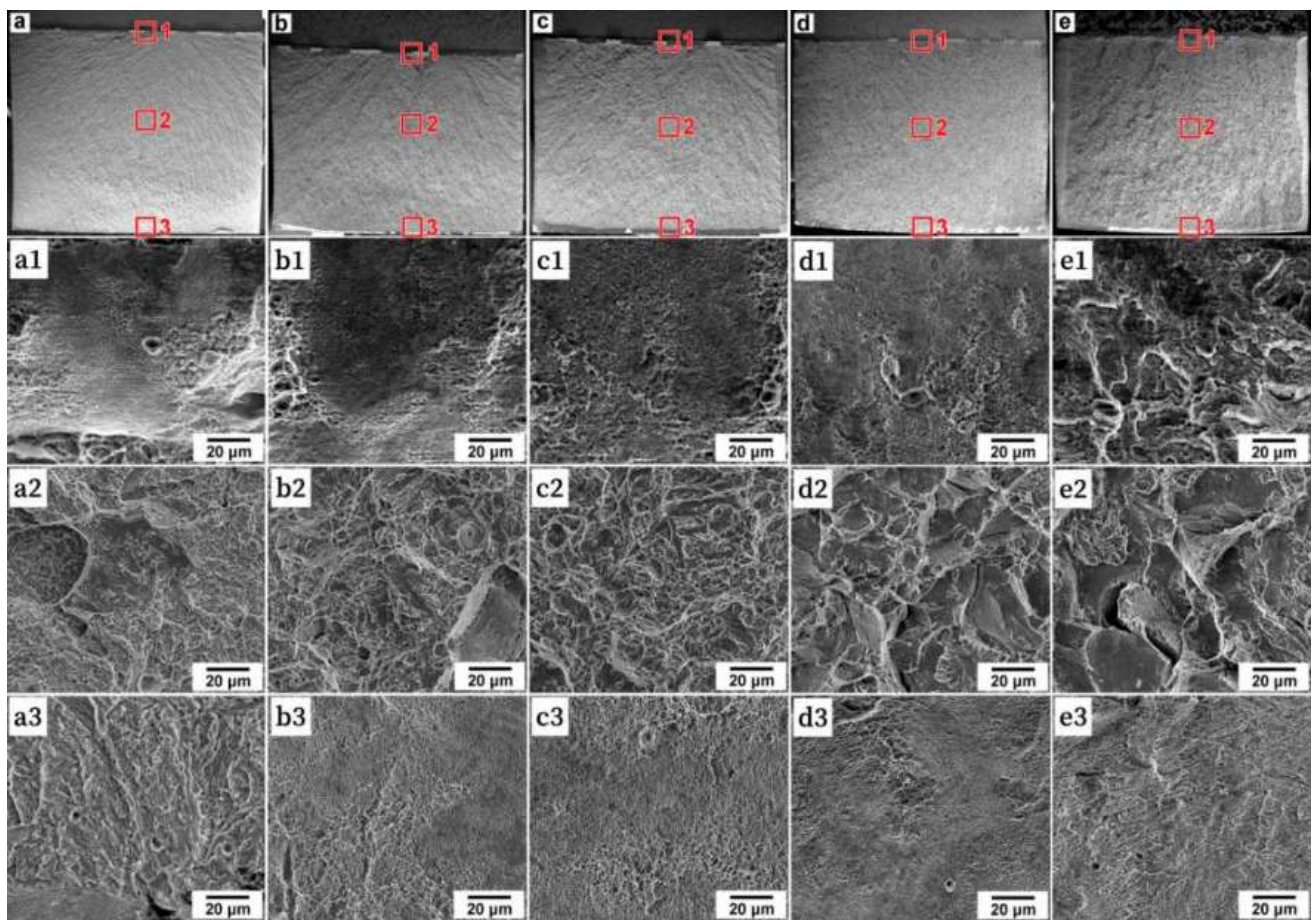


Figure 10. Low-magnification general view (a–e) and high-magnification fractographs of FCPZ (a1–e1) and SLZ (a2–e2) of the fracture surface in the Charpy V-notch specimens after water quenching (a–a2); tempering at 200 °C (b–b2), 280 °C (c–c2), 400 °C (d–d2), 500 °C (e–e2) of the Fe-0.34C steel.

Table 9. Effect of tempering on area fractions of initiation zone (IZ), fast crack propagation/fibrous zone (FCPZ) and shear-lip zone (SLZ).

Tempering Temperature, °C	IZ		FCPZ		SLZ	
	Fe-0.34C	Fe-0.44C	Fe-0.34C	Fe-0.44C	Fe-0.34C	Fe-0.44C
20	1	0.8	92	98	7	1.2
200	1.3	1.9	83	92	16	6
280	1.6	1.9	71	89	27	9
400	2.1	1.6	86	94	12	4.5
500	2.5	1.5	68	88	29	10

**Figure 11.** Low-magnification general view (a–e) and high-magnification fractographs of IZ (a1–e1), FCPZ (a2–e2) and SLZ (a3–e3) of the fracture surface in the Charpy V-notch specimens after water quenching (a–a3); tempering at 200 °C (b–b3), 280 °C (c–c3), 400 °C (d–d3), 500 °C (e–e3) of the Fe-0.44C steel.

Tempering at 200 °C increases the area fraction of the SLZ and contribution of dimple fracture in two steels (Figure 10(b1,b2) and Figure 11(b1–b3)). In the Fe-0.34C steel, the packets play a role of effective grain size for fracture in the FCPZ. Dimples are observed on tear ridges. In the Fe-0.44C steel, the cleavage occurs through whole packets in the FCPZ. The area fraction of dimple fracture tends to increase with the transition from the FCPZ to the SLZ. Blocks in coarse packets and fine packets play a role in the effective grain size for cleavage fracture in the FCPZ of the Fe-0.34C steel after tempering at 280 °C (Figure 10(c1)). The total area of the ductile fracture is high; a full dimple fracture takes place in the SLZ (Figure 10(c2)). Dimple fracture is observed in the IZ and SLZ in the Fe-0.44C steel (Figure 11(c1,c3)). Quasi-cleavage fracture with dense tear ridges is observed in the FCPZ (Figure 11(c2)).

Packet boundaries arrest the cleavage propagation in the FCPZ after tempering at 400 °C in the Fe-0.34C steel (Figure 10(d1)). Coherence length for cleavage fracture is restricted by block boundaries occasionally. Area fractions of the IZ and SLZ decrease (Table 9), but dimple fracture remains in these zones in two steels (Figures 10(d2) and 11(d1,d3)). In the Fe-0.44 the transition to intergranular brittle fracture along boundaries of PAGs occurs in the FCPZ (Figure 11(d2)). The amount of intergranular fracture increases with increasing carbon content. However, transgranular quasi-cleavage fracture remains dominant in this zone and a few intergranular facets are observed only. Tempering at 500 °C leads to decohesion along carbide/ferrite interfaces [46] in the IZ and SLZ in the Fe-0.34 steel (Figure 10(e2)), while dimple fracture could be also observed in these zones. In the FCPZ the transgranular quasi-cleavage fracture with PAGs as the effective grain size is in dominance, while cleavage within separate packets and even blocks could be rarely observed (Figure 10(e1)). Intergranular fracture plays a minor role in this zone in two steels. In the Fe-0.44C steel, the fine PAGs and packets in coarse PAGs play a role in the effective grain size for fracture in the FCPZ (Figure 11(e2)). Decohesion along carbide/ferrite interfaces is the main fracture mechanism in the IZ and SLZ (Figure 11(e1,e3)).

3.6. Cleavage Propagation in Martensite Lath Structure

Figure 12 shows the side views of the crack propagation in the CVN specimens of the Fe-0.34C steel. The EBSD maps clearly reveal that a crack propagates through the martensitic matrix across the numerous laths on the common cleavage planes after tempering at 280 °C, hence, confirming transgranular fracture (Figure 11a). The almost flat surface of crack propagation occurs within two coarse packets, whereas the rugged surfaces are observed for blocks with distinctly distinguished orientations. Therefore, cleavage may propagate along a $\{100\}_\alpha$ plane within a coarse packet, while propagation across blocks may lead to cleavage initiation along parallel $\{100\}_\alpha$ planes in adjacent blocks. The intersection of the crack propagation path with packets having the other $\{111\}_\gamma$ habit plane leads to the re-orientation of the crack path at an angle close to 90°; crack propagation redirects along a perpendicular $\{100\}_\alpha$ plane. Thus, block and packet/PAG boundaries serve as obstacles for crack propagation. However, cleavage propagation through block boundary leads to a transition to a parallel cleavage plane inclined to the primary cleavage plane at a small angle. The intersection of the propagation path with packet or PAG boundaries enables cleavage persistence along the other $\{100\}_\alpha$ plane. These boundaries redirect the crack propagation at a high angle in a cleavage manner.

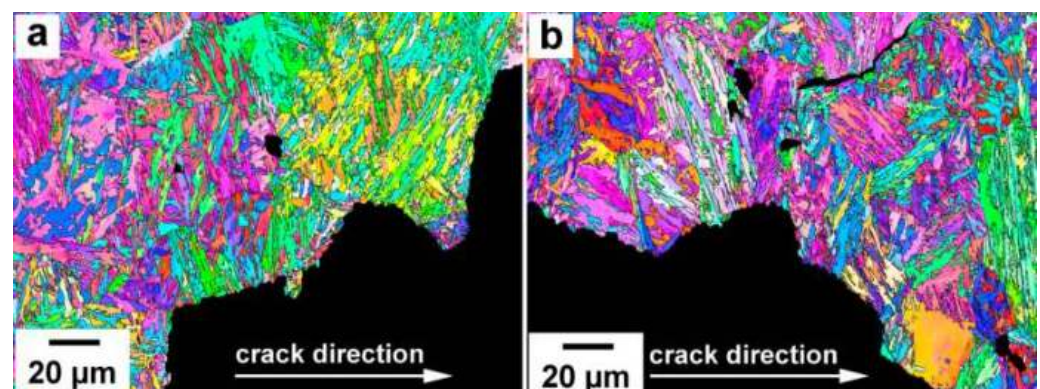


Figure 12. Profile fractograph of cleavage with misorientation maps in the FCPZ in the Fe-0.34C steel tempered at 280 °C (a) and 400 °C (b).

After tempering at 400 °C the flat surfaces at intersections of crack propagation path with block boundaries are in dominance (Figure 12b). The rugged surfaces are rarely observed. The zig-zag shape of the crack path is observed at areas of inclination of blocks with the other $\{111\}_\gamma$ habit plane to matrix of coarse packets containing, at least, six blocks belonging to a $\{111\}_\gamma$ habit plane. Crack effectively diverges at block

boundaries if neighboring blocks belong to different packets with two different $\{111\}_\gamma$ habit planes or K-S variants in two neighbor blocks with a packet with a common $\{111\}_\gamma$ habit plane are strongly misorientated [22]. This observation supports the conclusion of recent work [30]: the propagation of micro-crack stopped at the Bain unit boundaries. Therefore, only boundaries of the block bounded by a Bain unit may play a role of obstacles for cleavage propagation. TME is attributed to the fact that tempering at 400 °C eliminates the feasibility of block boundaries to play the role of obstacles for cleavage propagation. The facilitation of intergranular fracture along boundaries of a coarse PAG plays a minor role in the TME of the steel with ≥ 1.5 wt.%Si. Intergranular fracture remains incomplete and initiates crack propagation in a transgranular manner. After tempering at 280 °C, the crack path along the PAG boundary was rarely observed (Figure 12a). Thus, TME is attributed to the facilitation of transgranular fracture due to increased effective grain size for cleavage, mainly in Si-enriched low-alloy steels.

4. Discussion

4.1. Carbon Redistribution in Lath Martensite Structure and Quench Embrittlement

It is known [19,28,37] that carbon atoms tend to segregate along free dislocations and interfacial dislocations composing lath boundaries during quenching and the lath thickness has to ensure carbon segregation in Cottrell atmospheres. Carbon segregation in a lath boundary is controlled by the thickness of a Cottrell atmosphere, $d_{\text{Cottrell}} \sim 7$ nm and the mean lath thickness, d_{lath} [28,29,37,38]:

$$l_c = \sqrt{\frac{d_{\text{lath}}}{d_{\text{Cottrell}}}} b \quad (8)$$

$$X_{LB} = \left(\frac{b}{l_c}\right)^3 \quad (9)$$

where l_c is the mean carbon spacing, $b = 0.25$ is the magnitude of the Burgers vector in ferrite. The $X_{LB} = 0.0065$ and $X_{LB} = 0.0077$ calculated from Equations (8) and (9) are atomic fractions of carbon within the lath boundaries of the Fe-0.34 and Fe-0.44C steels, respectively. The $X_C = 0.0155$ and $X_C = 0.02$ are the total carbon content in at.% in the Fe-0.34 and Fe-0.44C steels, respectively. A portion of carbon segregated in lath boundaries in the form of Cottrell atmospheres and steel, V_{LB}^C , can be calculated from:

$$V_{LB}^C = \frac{X_{LB}}{X_C} \quad (10)$$

The $V_{LB}^C = 42\%$ and $V_{LB}^C = 38\%$ were obtained from Equation (10) for the Fe-0.34 and Fe-0.44C steels, respectively. It is worth noting that the Cottrell atmospheres evolve on free dislocations located within laths. No calculation of dislocation density by transmission electron microscopy was carried out in the present study. However, the density of free dislocations can be evaluated as about half of the interfacial dislocation density for Si-enriched low-alloy steel [29]. Therefore, about 63 and 57% of carbon atoms were consumed for the formation of Cottrell atmospheres in the Fe-0.34 and Fe-0.44C steels, respectively. The amount of carbon in solid solution may be 0.57 and 0.86 at.% in the Fe-0.34 and Fe-0.44C steels, respectively. However, it is known [28,29,50] that carbon content with martensite in the matrix is < 0.22 at.%. Therefore, excess carbon quantity is 0.35 and 0.64 at.% in the Fe-0.34 and Fe-0.44C steels, respectively, and this carbon may be consumed by HAB segregations [19,37,51] or may retain in the martensitic matrix. It was shown [19] that carbon excess at random HABs is higher than that at LABs by a factor of ~ 5 in medium-carbon low-alloy steel. However, coincidence site lattice (CSL) boundaries may attract significantly less carbon compared to random HABs [19]. It is known [22] that half-block boundaries are CSL boundaries. For the case of simplicity, we assume that only half of HABs in the lath martensite structure may attract carbon excess. In this case, the ratio

d_{lath}/d_{HAB} is 8.6 and 9.4 for the Fe-0.34C and Fe-0.44C steels, respectively (Tables 3 and 4). The $X_{HAB} = 0.0038$ and $X_{HAB} = 0.0040$ are atomic fractions of carbon within the HABs calculated for these ratios. It is seen that all excess carbon may segregate at dislocations and HABs in the Fe-0.34C steel, while 0.24 at.%C retain in the Fe-0.44C. Therefore, full saturation of boundary segregation takes place in this steel.

It is obvious that the superposition of saturated carbon segregation on PAG boundaries and carbon excess in the martensitic matrix results in quench embrittlement under static conditions due to the initiation of intergranular fracture in the Fe-0.44C. Under dynamic conditions, the initiation of quasi-cleavage fracture occurs at small fracture stress. Inspection of Equation (1) shows that very small fracture stress could be attributed to low γ_s value and, therefore, associated with carbon excess in the martensitic matrix [26,27]. In contrast with high-carbon steels containing >0.5 wt.%C [3,43] the quench embrittlement is eliminated by low-temperature tempering in the Si-enriched Fe-0.44 steel due to precipitation of transition carbides in the matrix instead of boundary cementite in medium-to-high carbon steels with low Si. The transition carbides consume an excess of carbon from boundary segregation and martensitic matrix that eliminates intergranular fracture under static conditions and increases cleavage fracture stress under dynamic conditions. Precipitation of transition carbides consumes carbon from Cottrell atmospheres and boundary segregations almost concurrently since the carbon segregation-driven reduction in grain boundary energy/segregation energy of ~ 79 kJ/mol [52,53] and interaction energy between carbon atoms and dislocations of ~ 70 kJ/mol [54,55] are nearly the same. It is worth noting that a 0.43 wt.%C steel with nearly the same substitutional alloying element exhibited a very high density of free lattice dislocation ($1.5 \times 10^{15} \text{ m}^{-2}$) in the as-quenched condition and showed no quench embrittlement under static condition [20]. Therefore, a strong increase in sites for redistribution of carbon from the martensitic matrix to Cottrell atmospheres that reduces carbon excess in the martensitic matrix and on HABs is efficient in suppression of quench embrittlement.

In addition, some carbon atoms are located in RA [37]. However, the volume fraction of RA is negligible in both steels and, therefore, the quantity of carbon redistributed in RA will not be taken into account in the present consideration.

4.2. Mechanism of Tempered Martensite Embrittlement

TME is attributed to a combination of three factors in the steels with ≥ 1.5 wt.%Si. TME is associated with increased effective grain size for cleavage fracture, d_{eff} , mainly. This is the first factor. Transition in the coherence length for cleavage fracture from the level of fine packets or blocks in coarse packets after tempering at 280 °C to the level of coarse packets and fine PAGs after tempering at 400 °C takes place in the Si-enriched steels. Cleavage propagation occurs through the majority of block boundaries after tempering at 400 °C which increases the d_{eff} value and, therefore, decreases fracture stress in accordance with Equation (1). Inspection of experimental data shows that block boundaries may arrest the cleavage propagation if carbon segregates at these boundaries after quenching or low-temperature tempering and/or film-like RA locates on block boundaries. In addition, block boundaries serve as obstacles for cleavage propagation if chains of cementite particles precipitate at these boundaries after tempering at 500 °C. Precipitation of transition carbides consumes the carbon segregations on block boundaries and decomposition of RA after tempering at 400 °C. As a result, cleavage propagates through these boundaries. This is a unique mechanism of TME in the steels with ≥ 1.5 wt.%Si.

Coarsening of η -Fe₂C carbides may facilitate transgranular cleavage due to void formation at its interfaces [35]. This is the second factor. It is apparent that carbon content in the martensitic matrix is retained at a relatively high level that provides a relatively high work hardening rate. However, the volume fraction of transition η -Fe₂C carbides serving as obstacles for dislocation glide increases with increasing temperature of tempering that decreases uniform elongation. UTS value is attained at lower strains after tempering at 400 °C which leads to low PSE. The strong effect of TME on ductility and the PSE in the

Fe-0.44C steel is associated with the fact that the values of σ_F and UTS become nearly the same and the onset of immediate fracture takes place at UTS. Therefore, a decrease in elongation to failure after tempering at 400 °C also associates with TME.

The transgranular fracture plays a major role and the role of intergranular fracture is insignificant in TME. No precipitation of boundary cementite occurs in the Si-enriched steels examined that strongly diminishes the severity of TME. Intergranular fracture is attributed to a specific embrittling agent. This is the third factor. Intergranular fracture is associated with the precipitation of relatively coarse transition η -Fe₂C carbides in the vicinity of the packet and PAG boundaries owing to the decomposition of RA. The coarse plates of η -Fe₂C carbide facilitate crack propagation along boundaries of packets and PAGs but no transition from transgranular fracture to intergranular one occurs. It is worth noting that authors [14,23] assumed that interlath cementite plays the role of the embrittling agent in Si-enriched 300M steel under low-temperature tempering. However, this presumption was not supported by structural characterization [14,23].

After tempering at 500 °C, the precipitation of boundary cementite considered an embrittling agent responsible for TME [3,6,48] takes place in the Si-rich steels. Fractography observations prove irrefutably the decohesion along carbide/ferrite interfaces [37]. However, this process promotes intergranular fracture slightly. It is apparent that full carbon depletion from martensite takes place at this tempering temperature and the ferritic matrix is characterized by a high surface energy of the cleavage plane [18–20,35] that highly increases fracture stress, σ_F , in accordance with Equation (1). Therefore, boundary cementite may play the role of an effective embrittling agent responsible for TME, if this phase precipitates in martensitic matrix, only. Thus, the elimination of overlap between Stages I and III of tempering due to the replacement of cementite by transition η -Fe₂C carbide in low-alloy steel with Si \geq 1.5 wt.% highly diminishes the severity of TME.

5. Conclusions

1. Quench embrittlement in an as-quenched condition defined as a drop in room temperature ductility and low value the Charpy V-notch impact absorbed energy in the Fe-0.44C steel associates with intergranular fracture under static conditions and small fracture stress for transgranular fracture under dynamic conditions. Quench embrittlement appears in steels with Si \geq 1.5 wt.% if no full redistribution of carbon to Cottrell atmospheres and boundary segregation occurs during quenching and a high carbon excess retains in the martensitic matrix. Quench embrittlement is diminished by low-temperature tempering due to precipitation transition η -Fe₂C carbide that leads to carbon depletion from boundary segregations and martensitic matrix.

2. Tempered martensite embrittlement in Si-enriched medium-carbon low-alloy steels defined as decreases in elongation-to-failure, the product of strength and elongation (PSE), $\sigma_B \cdot \delta$ (MPa \times %) and the Charpy V-notch impact absorbed energy takes place in the Fe-0.34 and Fe-0.44C low-alloy steels with Si $>$ 1.5 wt.% after tempering at 400 °C due to superposition of increased effective grain size for brittle fracture, coarsening particles of transition η -Fe₂C carbide and facilitation of intergranular fracture. Intergranular fracture associated with precipitation of coarse η -Fe₂C carbide in the vicinity of the packet and PAG boundaries due to the decomposition of retained austenite plays an insignificant role in tempered martensite embrittlement. Additions of Si $>$ 1.5 wt.% in low-alloy steels decrease the severity of tempered martensite embrittlement due to the suppression of cementite precipitation on boundaries.

3. Boundary cementite may play the role of embrittling agent for tempered martensite embrittlement if this phase precipitates at boundaries and transition carbides precipitate in martensitic matrix, concurrently. At a tempering temperature of 500 °C, precipitation of cementite on low- and high-angle boundaries of ferrite leads to increased ductility and the Charpy V-notch impact absorbed energy despite decohesion along carbide/ferrite interfaces.

Author Contributions: Conceptualization, R.M. and R.K.; methodology, R.M. and Y.B.; validation, Y.B. and S.G.; formal analysis, Y.B.; investigation, R.M., Y.B., S.G., T.K. and R.K.; resources, R.K.; data curation, Y.B. and R.M.; writing—original draft preparation, R.K.; writing—review and editing, Y.B. and R.M.; visualization, Y.B. and R.M.; supervision, R.K.; project administration, R.K.; funding acquisition, R.K. All authors have read and agreed to the published version of the manuscript.

Funding: This research was funded by the Ministry of Science and Higher Education of the Russian Federation, grant number 075-15-2021-572.

Data Availability Statement: Not applicable.

Acknowledgments: The studies were carried out on the equipment of the Joint Scientific Center for Technologies and Materials of Belgorod State National Research University, which was supported by the Ministry of Science and Higher Education of the Russian Federation under contract No. 075-15-2021-690 (unique identifier RF-2296.61321X0030).

Conflicts of Interest: The authors declare no conflict of interest.

Abbreviations

YS	yield stress
UHSS	ultra-high-strength steels
CVN	Charpy V-notch
RA	retained austenite
Q&P processing	quenching and partitioning processing
TME	tempered martensite embrittlement
PAG	prior austenite grains
σ_F	fracture stress
γ_s	surface energy of the cleavage plane
d_{eff}	effective grain size
Q&T	austenitizing followed by quenching and tempering treatment
SEM	scanning electron microscope
TEM	transmission electron microscope
EBSD	electron backscatter diffraction
LAB	low-angle boundary
HAB	high-angle boundary
DSC	differential scanning calorimetry
M_S	martensite start temperature
M_F	martensite finish temperature
D_{packet}	average dimension of packets
D_{PAG}	average dimension of PAGs
N_p	number of packets in a PAG
d_{block}	average dimension of blocks
N_b	number of blocks in a packet
K–S	Kurdjumov–Sachs
OR	orientation relationship
ρ_{KAM}	densities of lattice dislocations were calculated from misorientation maps obtained by EBSD technique using Kernel average misorientation
AR	aspect ratio
UTS	ultimate tensile strength
PSE	product of strength and elongation
El_u	uniform elongation
El_t	total elongation
P_m	maximum load
YS	yield stress
DUTS	dynamic ultimate tensile strength
IZ	initiation zone
FCPZ	fast crack propagation/fibrous zone

SLZ	shear-lip zone
d_{Cottrell}	thickness of a Cottrell atmosphere
d_{lath}	mean lath thickness
V_{LB}^{C}	portion of carbon segregated in lath boundaries in the form of Cottrell atmospheres
CSL	coincidence site lattice

Appendix A Structural Characteristics of the Fe-0.34C Steel

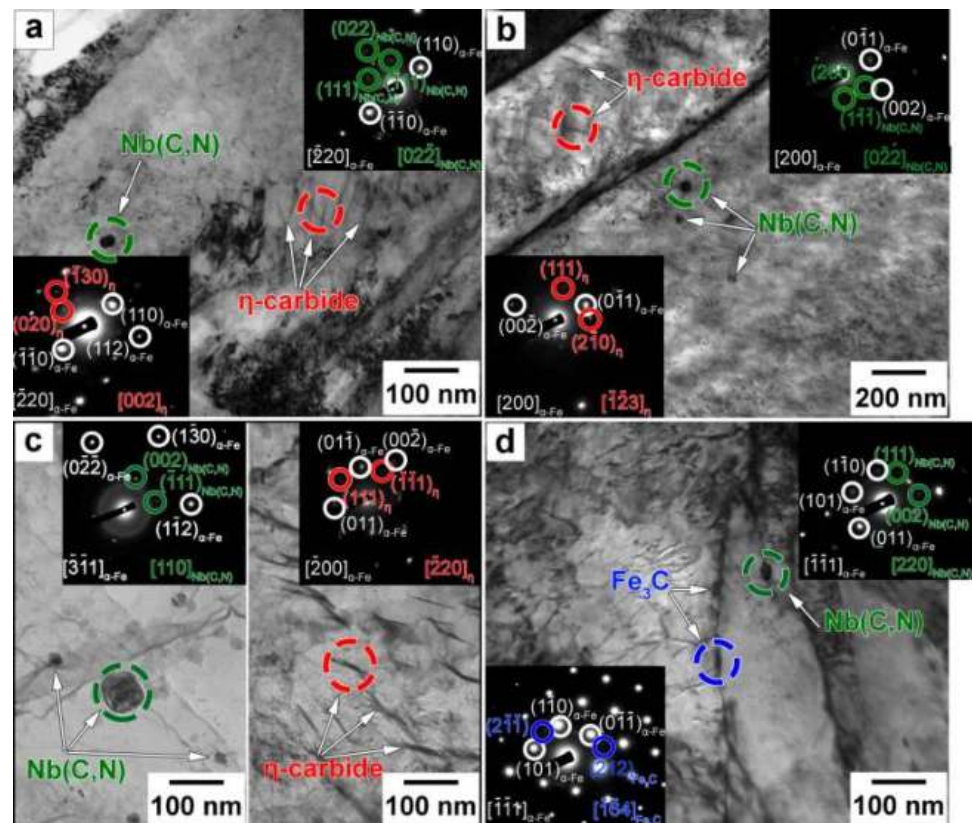


Figure A1. Typical TEM micrograph of the Fe-0.34C steel after quenching (a); tempering at 200 °C (b); 400 °C (c); and 500 °C (d).

Table A1. Effect of tempering on dimensions of secondary phase particles in the Fe-0.34C steel.

Tempering Temperature, °C	Size of Nb(C,N), nm	Dimensions of η -Fe ₂ C, nm	Size of Fe ₃ C, nm
20	27	40/5	-
200	33	73/6 *	-
280	34	120/7	-
400	34	132/7	-
500	48	-	26

* Numerator and denominator are the particle length and thickness, respectively.

References

- Malakondaiah, G.; Srinivas, M.; Rao, P. Ultrahigh-strength low-alloy steels with enhanced fracture toughness. *Prog. Mater. Sci.* **1997**, *42*, 209–242. [[CrossRef](#)]
- Li, J.; Zhan, D.; Jiang, Z.; Zhang, H.; Yang, Y.; Zhang, Y. Progress on improving strength-toughness of ultra-high strength martensitic steels for aerospace applications: A review. *J. Mater. Res. Technol.* **2023**, *23*, 172–190. [[CrossRef](#)]
- Krauss, G. *Steels: Processing Structure, and Performance*, 2nd ed.; ASM International: Materials Park, OH, USA, 2005.
- Teramoto, S.; Imura, M.; Masuda, Y.; Ishida, T.; Ohnuma, M.; Neishi, Y.; Suzuki, T. Influence of Iron Carbide on Mechanical Properties in High Silicon-added Medium-carbon Martensitic Steels. *Iron Steel Inst. Jpn. Int.* **2020**, *60*, 182–189. [[CrossRef](#)]

5. Tsuboi, M.; Shibata, A.; Terada, D.; Tsuji, N. Role of Different Kinds of Boundaries Against Cleavage Crack Propagation in Low-Temperature Embrittlement of Low-Carbon Martensitic Steel. *Met. Mater. Trans. A* **2017**, *48*, 3261–3268. [[CrossRef](#)]
6. Zia-Ebrahimi, F.; Krauss, G. Mechanisms of tempered martensite embrittlement in medium-carbon steels. *Acta Met.* **1984**, *32*, 1767–1778. [[CrossRef](#)]
7. Clarke, A.J.; Klemm-Toole, J.; Clarke, K.D.; Coughlin, D.R.; Pierce, D.T.; Euser, V.K.; Poplawsky, J.D.; Clausen, B.; Brown, D.; Almer, J.; et al. Perspectives on quenching and tempering 4340 steel. *Metall. Mater. Trans. A* **2020**, *51*, 4984–5005. [[CrossRef](#)]
8. Tomita, Y. Development of fracture toughness of ultrahigh strength, medium carbon, low alloy steels for aerospace applications. *Int. Mater. Rev.* **2000**, *45*, 27–37. [[CrossRef](#)]
9. Manokaran, M.; Kashinath, A.S.; Jha, J.S.; Toppo, S.P.; Singh, R.P. Influence of Tempering in Different Melting Routes on Toughness Behavior of AISI 4340 Steel. *J. Mater. Eng. Perform.* **2020**, *29*, 6748–6760. [[CrossRef](#)]
10. Euser, V.K.; Williamson, D.L.; Clarke, A.J.; Speer, J.G. Cementite Precipitation in Conventionally and Rapidly Tempered 4340 Steel. *JOM* **2022**, *74*, 2386–2394. [[CrossRef](#)]
11. Tikhe, O.; Doiphode, P.; Nichul, U.; Singh, R.; Hiwarkar, V. Development of Optimized Mechanical Properties of AISI 4340 Steel: Role of Quenching and Partitioning Process. *Met. Mater. Int.* **2023**, *29*, 2216–2227. [[CrossRef](#)]
12. Nam, W.-J.; Choi, H.-C. Effects of silicon, nickel, and vanadium on impact toughness in spring steels. *Mater. Sci. Technol.* **1997**, *13*, 568–574. [[CrossRef](#)]
13. Salvetr, P.; Gokhman, A.; Nový, Z.; Motyčka, P.; Kotous, J. Effect of 1.5 wt% Copper Addition and Various Contents of Silicon on Mechanical Properties of 1.7102 Medium Carbon Steel. *Materials* **2021**, *14*, 5244. [[CrossRef](#)]
14. Euser, V.K.; Williamson, D.L.; Findley, K.O.; Clarke, A.J.; Speer, J.G. The Role of Retained Austenite in Tempered Martensite Embrittlement of 4340 and 300-M Steels Investigated through Rapid Tempering. *Metals* **2021**, *11*, 1349. [[CrossRef](#)]
15. Salvetr, P.; Školáková, A.; Kotous, J.; Drahokoupil, J.; Melzer, D.; Jansa, Z.; Donik, Č.; Gokhman, A.; Nový, Z. Effect of Double-Step and Strain-Assisted Tempering on Properties of Medium-Carbon Steel. *Materials* **2023**, *16*, 2121. [[CrossRef](#)] [[PubMed](#)]
16. Tkachev, E.; Borisov, S.; Borisova, Y.; Kniazziuk, T.; Gaidar, S.; Kaibyshev, R. Strength–Toughness of a Low-Alloy 0.25C Steel Treated by Q&P Processing. *Materials* **2023**, *16*, 3851. [[CrossRef](#)]
17. Yuzbekova, D.; Dudko, V.; Pydrin, A.; Gaidar, S.; Mironov, S.; Kaibyshev, R. Effect of Tempforming on Strength and Toughness of Medium-Carbon Low-Alloy Steel. *Materials* **2023**, *16*, 1202. [[CrossRef](#)]
18. Peters, J.; Bee, J.; Kolk, B.; Garrett, G. On the mechanisms of tempered martensite embrittlement. *Acta Met.* **1989**, *37*, 675–686. [[CrossRef](#)]
19. Morsdorf, L.; Kashiwar, A.; Kübel, C.; Tasan, C. Carbon segregation and cementite precipitation at grain boundaries in quenched and tempered lath martensite. *Mater. Sci. Eng. A* **2023**, *862*, 144369. [[CrossRef](#)]
20. Dudko, V.; Yuzbekova, D.; Gaidar, S.; Vetrova, S.; Kaibyshev, R. Tempering Behavior of Novel Low-Alloy High-Strength Steel. *Metals* **2022**, *12*, 2177. [[CrossRef](#)]
21. Fedorova, I.; Kostka, A.; Tkachev, E.; Belyakov, A.; Kaibyshev, R. Tempering behavior of a low nitrogen boron-added 9%Cr steel. *Mater. Sci. Eng. A* **2016**, *662*, 443–455. [[CrossRef](#)]
22. Kitahara, H.; Ueji, R.; Tsuji, N.; Minamino, Y. Crystallographic features of lath martensite in low-carbon steel. *Acta Mater.* **2006**, *54*, 1279–1288. [[CrossRef](#)]
23. Euser, V.K.; Williamson, D.L.; Clarke, A.J.; Speer, J.G. Limiting Retained Austenite Decomposition in Quenched and Tempered Steels: Influences of Rapid Tempering and Silicon. *Iron Steel Inst. Jpn. Int.* **2020**, *60*, 2990–3000. [[CrossRef](#)]
24. Bhadeshia, H.K.D.H. Physical Metallurgy of Steels. In *Physical Metallurgy*; Laughlin, D.E., Hono, K., Eds.; Elsevier: Amsterdam, The Netherlands, 2014; pp. 2157–2214. [[CrossRef](#)]
25. Hanamura, T.; Yin, F.; Nagai, K. Ductile–Brittle Transition Temperature of Ultrafine Ferrite/Cementite Microstructure in a Low Carbon Steel Controlled by Effective Grain Size. *Iron Steel Inst. Jpn. Int.* **2004**, *44*, 610–617. [[CrossRef](#)]
26. Inoue, T.; Qiu, H.; Ueji, R.; Kimura, Y. Ductile-to-Brittle Transition and Brittle Fracture Stress of Ultrafine-Grained Low-Carbon Steel. *Materials* **2021**, *14*, 1634. [[CrossRef](#)]
27. Morris, J.J.W. On the Ductile–Brittle Transition in Lath Martensitic Steel. *Iron Steel Inst. Jpn. Int.* **2011**, *51*, 1569–1575. [[CrossRef](#)]
28. Galindo-Nava, E.; Rivera-Díaz-Del-Castillo, P. A model for the microstructure behaviour and strength evolution in lath martensite. *Acta Mater.* **2015**, *98*, 81–93. [[CrossRef](#)]
29. Tkachev, E.; Borisov, S.; Belyakov, A.; Kniazziuk, T.; Vagina, O.; Gaidar, S.; Kaibyshev, R. Effect of quenching and tempering on structure and mechanical properties of a low-alloy 0.25C steel. *Mater. Sci. Eng. A* **2023**, *868*, 144757. [[CrossRef](#)]
30. Shibata, A.; Katsuno, T.; Tsuboi, M.; Tsuji, N. Effect of Bain unit size on low-temperature fracture toughness in medium-carbon martensitic and bainitic steels. *Iron Steel Inst. Jpn. Int.* **2023**. [[CrossRef](#)]
31. Javaheri, V.; Pallaspuro, S.; Sadeghpour, S.; Ghosh, S.; Sainio, J.; Latypova, R.; Kömi, J. Rapid tempering of a medium-carbon martensitic steel: In-depth exploration of the microstructure—Mechanical property evolution. *Mater. Des.* **2023**, *231*, 112059. [[CrossRef](#)]
32. Calcagnotto, M.; Ponge, D.; Demir, E.; Raabe, D. Orientation gradients and geometrically necessary dislocations in ultrafine grained dual-phase steels studied by 2D and 3D EBSD. *Mater. Sci. Eng. A* **2010**, *527*, 2738–2746. [[CrossRef](#)]
33. Niessen, F.; Nyyssönen, T.; Gazder, A.A.; Hielscher, R. Parent grain reconstruction from partially or fully transformed microstructures in MTEX. *J. Appl. Crystallogr.* **2022**, *55*, 180–194. [[CrossRef](#)]

34. Miyamoto, G.; Iwata, N.; Takayama, N.; Furuhashi, T. Mapping the parent austenite orientation reconstructed from the orientation of martensite by EBSD and its application to ausformed martensite. *Acta Mater.* **2010**, *58*, 6393–6403. [[CrossRef](#)]
35. Mishnev, R.; Dudova, N.; Dudko, V.; Kaibyshev, R. Impact toughness of a 10% Cr steel with high boron and low nitrogen contents. *Mater. Sci. Eng. A* **2018**, *730*, 1–9. [[CrossRef](#)]
36. Borisova, Y.; Mishnev, R.; Tkachev, E.; Kniaziuk, T.; Gaidar, S.; Kaibyshev, R. Structure, phase composition and mechanical properties of high strength steel with transition h-Fe₂C carbide. *Physic Met. Metallogr.* **2023**; *accepted for publication*.
37. Galindo-Nava, E.; Rainforth, W.; Rivera-Díaz-Del-Castillo, P. Predicting microstructure and strength of maraging steels: Elemental optimisation. *Acta Mater.* **2016**, *117*, 270–285. [[CrossRef](#)]
38. Galindo-Nava, E. On the prediction of martensite formation in metals. *Scr. Mater.* **2017**, *138*, 6–11. [[CrossRef](#)]
39. Shibata, A.; Miyamoto, G.; Morito, S.; Nakamura, A.; Moronaga, T.; Kitano, H.; Gutierrez-Urrutia, I.; Hara, T.; Tsuzaki, K. Substructure and crystallography of lath martensite in as-quenched interstitial-free steel and low-carbon steel. *Acta Mater.* **2023**, *246*, 118675. [[CrossRef](#)]
40. Vervynck, S.; Verbeken, K.; Lopez, B.; Jonas, J.J. Modern HSLA steels and role of non-recrystallisation temperature. *Int. Mater. Rev.* **2012**, *57*, 187–207. [[CrossRef](#)]
41. Ning, D.; Dai, C.; Wu, J.; Wang, Y.; Jing, Y.; Sun, J. Carbide precipitation and coarsening kinetics in low carbon and low alloy steel during quenching and subsequently tempering. *Mater. Charact.* **2021**, *176*, 111111. [[CrossRef](#)]
42. Porter, D.A.; Easterling, K.E.; Sherif, M. *Phase Transformation in Metals and Alloys*, 3rd ed.; CRS Press: Boca Raton, FL, USA, 2009; ISBN 978-1-4398-8357-0.
43. Reguly, A.; Strohaecker, T.R.; Krauss, G.; Matlock, D.K. Quench embrittlement of hardened 5160 steel as a function of austenitizing temperature. *Met. Mater. Trans. A* **2004**, *35*, 153–162. [[CrossRef](#)]
44. ASM International. *A.S.M. Handbook: Mechanical Testing and Evaluation*; ASM International: New York, NY, USA, 2000.
45. Chaouadi, R.; Gérard, R. Development of a method for extracting fracture toughness from instrumented Charpy impact tests in the ductile and transition regimes. *Theor. Appl. Fract. Mech.* **2021**, *115*, 103080. [[CrossRef](#)]
46. Mills, K.; Davis, J.R.; Destefani, J.D.; Dieterich, D. *ASM Handbook. Fractography*; ASM International: Materials Park, OH, USA, 1987; Volume 12.
47. Dudko, V.; Fedoseeva, A.; Kaibyshev, R. Ductile-brittle transition in a 9% Cr heat-resistant steel. *Mater. Sci. Eng. A* **2016**, *682*, 73–84. [[CrossRef](#)]
48. Mishnev, R.; Dudova, N.; Kaibyshev, R.; Belyakov, A. On the Fracture Behavior of a Creep Resistant 10% Cr Steel with High Boron and Low Nitrogen Contents at Low Temperatures. *Materials* **2020**, *13*, 3. [[CrossRef](#)]
49. Wang, Q.; Ye, Q.; Wang, Z.; Kan, L.; Wang, H. Thickness Effect on Microstructure, Strength, and Toughness of a Quenched and Tempered 178 mm Thickness Steel Plate. *Metals* **2020**, *10*, 572. [[CrossRef](#)]
50. Hutchinson, B.; Hagström, J.; Karlsson, O.; Lindell, D.; Tornberg, M.; Lindberg, F.; Thuvander, M. Microstructures and hardness of as-quenched martensites (0.1–0.5% C). *Acta Mater.* **2011**, *59*, 5845–5858. [[CrossRef](#)]
51. Seehaus, M.; Korte-Kerzel, S.; Sandlöbes-Haut, S. Influence of Si on the microstructure and C redistribution in martensitic steels. *Mater. Des.* **2023**, *229*, 111875. [[CrossRef](#)]
52. Raabe, D.; Herbig, M.; Sandlöbes, S.; Li, Y.; Tytko, D.; Kuzmina, M.; Ponge, D.; Choi, P.-P. Grain boundary segregation engineering in metallic alloys: A pathway to the design of interfaces. *Curr. Opin. Solid State Mater. Sci.* **2014**, *18*, 253–261. [[CrossRef](#)]
53. Lejček, P.; Šob, M.; Paidar, V. Interfacial segregation and grain boundary embrittlement: An overview and critical assessment of experimental data and calculated results. *Prog. Mater. Sci.* **2017**, *87*, 83–139. [[CrossRef](#)]
54. Wilde, J.; Cerezo, A.; Smith, G. Three-dimensional atomic-scale mapping of a Cottrell atmosphere around a dislocation in iron. *Scr. Mater.* **2000**, *43*, 39–48. [[CrossRef](#)]
55. Lejček, P.; Hofmann, S.; Paidar, V. The Significance of Entropy in Grain Boundary Segregation. *Materials* **2019**, *12*, 492. [[CrossRef](#)]

Disclaimer/Publisher’s Note: The statements, opinions and data contained in all publications are solely those of the individual author(s) and contributor(s) and not of MDPI and/or the editor(s). MDPI and/or the editor(s) disclaim responsibility for any injury to people or property resulting from any ideas, methods, instructions or products referred to in the content.